



1 Stress Characterization and Temporal Evolution of Borehole Failure 2 at the Rittershoffen Geothermal Project

3
4 Jérôme Azzola¹, Benoît Valley², Jean Schmittbuhl¹, Albert Genter³

5 ¹Institut de Physique du Globe de Strasbourg/EOST, University of Strasbourg/CNRS, Strasbourg, France

6 ²Center for Hydrogeology and Geothermics, University of Neuchâtel, Neuchâtel, Switzerland

7 ³ÉS géothermie, Schiltigheim, France

8 *Correspondence to:* Jérôme Azzola (azzola@unistra.fr)

9 **Abstract.** In the Upper Rhine Graben, several innovative projects based on the Enhanced Geothermal System (EGS)
10 technology exploit local deep fractured geothermal reservoirs. The principle underlying this technology consists of
11 increasing the hydraulic performances of the natural fractures using different stimulation methods in order to circulate the
12 natural brine with commercially flow rates. For this purpose, the knowledge of the *in-situ* stress state is of central importance
13 to predict the response of the rock mass to the different stimulation programs. Here, we propose a characterization of the *in-*
14 *situ* stress state from the analysis of Ultrasonic Borehole Imager (UBI) data acquired at different key moments of the
15 reservoir development using a specific image correlation technique. This unique dataset has been obtained from the open
16 hole sections of the two deep wells (GRT-1 and GRT2, ~2500m) at the geothermal site of Rittershoffen, France. We based
17 our analysis on the geometry of breakouts and of drilling induced tension fractures (DITF). A transitional stress regime
18 between strike-slip and normal faulting consistently with the neighbour site of Soultz-sous-Forêts is evidenced. The time
19 lapse dataset enables to analyse both in time and space the evolution of the structures over two years after drilling. The
20 image correlation approach developed for time lapse UBI images shows that breakouts extend along the borehole with time,
21 widen (i.e. angular opening between the edges of the breakouts) but do not deepen (i.e. increase of the maximal radius of the
22 breakouts). The breakout widening is explained by wellbore thermal equilibration. A significant stress rotation at depth is
23 evidenced. It is shown to be controlled by a major fault zone and not by the sediment-basement interface. Our analysis does
24 not reveal any significant change in the stress magnitude in the reservoir.



25 1 Introduction

26 Several deep geothermal projects located in the Upper Rhine Graben and based on the Enhanced Geothermal System (EGS)
27 technology exploit local geothermal reservoirs, such as those located in Soultz-sous-Forêts or in Rittershoffen (Baujard et al.,
28 2017; Genter et al., 2010). The principle underlying this technology consists of increasing the hydraulic performance of the
29 reservoir through different types of stimulations to achieve commercially interesting flow rates. The stimulation techniques
30 are typically based on high pressure injection (hydraulic stimulation), cold water injection (thermal stimulation) or chemical
31 injection (chemical stimulation). During the injections, a thermo-hydro-chemo-mechanical perturbation induces an increase
32 in permeability due to the reactivation of existing structures or the generation of new ones (Cornet, 2015; Huenges & Ledru,
33 2011). The *in-situ* stress state is a key parameter controlling rock mass response during stimulation and is required to design
34 stimulation strategies and forecast the response of the reservoir to varying injection schemes.

35 Despite its importance, the *in-situ* stress state is difficult to assess, particularly in situations where the rock mass is only
36 accessible through a few deep boreholes. In such cases, the assessment of borehole walls using borehole logging imaging is a
37 useful technique to provide information on the type, the orientation and the size of fractures or breakouts which are owed to
38 the stress perturbations related to existence of the well (drilling and fluid boundary conditions). Subsequently, it gives useful
39 constraints on the *in-situ* stress state surrounding the wellbore (Schmitt et al., 2012; Zoback et al., 2003). Borehole breakouts
40 provide a indirect information on the stress orientation that it is difficult to extract in particular for robust quantitative stress
41 magnitudes. Indeed, it relies on the choice of the failure model used to interpret borehole wall images. Indeed, the
42 mechanisms that control the failure evolution of the borehole wall are not well understood both in space and time, and there
43 is no consensus on the most appropriate failure criteria to be used. Parameterizing failure criteria is also a challenge since
44 intact core material is often not available from deep boreholes. Finally, the set of images used to identify borehole failures is
45 typically acquired a few days after drilling completion when it is unclear if the geometry has reached a new stationary state
46 yet. The present analysis addresses these difficulties as we attempt to characterise the stress state at the Rittershoffen
47 geothermal site (France).

48 We first present in this paper the geological and geodynamical context of the Rittershoffen geothermal site (France). We
49 describe the borehole imaging data acquired in the GRT-1 and GRT-2 wells at the Rittershoffen geothermal project. We then
50 proceed to a brief review of the methods used for UBI analyses with their underlying assumptions. We applied the
51 methodology proposed by Schmitt et al. (2012) and Zoback et al. (2003) in order to assess the stress state at this site. To
52 analyse the three successive images of the wellbore acquired up to two years after drilling completion, we developed an
53 image processing method of the UBI data to compare in time the geometry of breakouts. We deduce from this study, the
54 evolution of breakouts with time and evaluate its impact on our *in-situ* stress state assessment. We finally propose our best
55 estimate of the *in-situ* stress state for the Rittershoffen site, both in orientation and magnitude.



56 2 Rittershoffen project context

57 The Rittershoffen geothermal project, also referred as the ECOGI Project is located near the village of Rittershoffen in
58 North-Eastern France (Alsace). It is an EGS geothermal project initiated in 2011 (Baujard et al., 2015, 2017). The doublet
59 has been drilled between Rittershoffen and Betschdorf, 6 km east of the Soultz-sous-Forêts geothermal project, in the
60 Northern Alsace, France (Genter et al., 2010). The aim of the project is to deliver heat through a long pipeline loop to the
61 “Roquette Frères” bio-refinery located 15 km apart. The power plant capacity is 24 MWth, intending to cover up to 25% of
62 the client heat need. Figure 1 gives an overview of the project location and presents in the right insert the trajectory and
63 completion of the two wells GRT-1 and GRT-2 that have been drilled (Baujard et al, 2017). GRT-1 was completed in
64 December 2013. It was drilled to a depth of 2580 m (MD, depth measured along hole) corresponding to a vertical depth
65 (TVD) of 2562 m. The well penetrates the crystalline basement at a depth of 2212 m MD and targets a local complex fault
66 structure (Baujard et al., 2017; Lengliné et al., 2017; Vidal et al., 2016). The 8” 1/2 diameter open-hole section of the well
67 starts at 1922 m MD. The borehole is almost vertical with a maximum deviation of 9° only. The first hydraulic tests
68 concluded in an insufficient injectivity of the injection well GRT-1. Therefore, the well was stimulated in 2013, which
69 resulted in a fivefold increase of the injectivity (Baujard et al., 2017). The target of the production well GRT-2 and its
70 trajectory have been designed benefiting from the results of additional seismic profiles acquired in the meantime. GRT-2
71 targets the same fault structure but more than one kilometre away from GRT-1. Local complexities of the fault structure as
72 ‘in steps’ geometry, has been observed *a-posteriori* from the micro-seismic monitoring during GRT-1 stimulation
73 (Lengliné et al, 2017). The GRT-2 borehole was drilled in 2014 to a total depth of 3196 m MD (2708 m TVD) (Baujard et
74 al., 2017). The granite basement is penetrated at a depth of 2493.5 m MD. The 8” 1/2 diameter open-hole section starts at a
75 depth of 2120 m MD. This borehole is strongly deviated with a mean deviation of 37° over the interval of interest.

76 The left insert of Figure 1 shows more specifically the geological units penetrated by the deep boreholes of the geothermal
77 sites in Rittershoffen and Soultz-sous-Forêts. It consists of sedimentary layers from the Cenozoic and Mesozoic that are
78 overlaying a crystalline basement made of altered and fractured granitic rocks (Aichholzer et al., 2016). Natural fractures are
79 well developed in the Vosges sandstones and Annweiler sandstones, as in the granitic basement. Oil and Gas exploration in
80 the area led to a good knowledge of the regional sub-surface including measures of temperatures at depth. The unusual high
81 geothermal gradient encountered in Soultz-sous-Forêts which is one of the largest described so far in the Upper Rhine
82 graben, encouraged the development of the ECOGI project in this area (Baujard et al, 2017).

83 The geological context is characterized in the vicinity of the Soultz-sous-Forêts and Rittershoffen sites from numerous
84 studies owing to the extended geophysical exploration in the region (Aichholzer et al., 2016; Cornet et al., 2007;
85 Dezayes et al., 2005; Dorbath et al., 2010; Evans et al., 2009; Genter et al., 2010; Rummel, 1991; Rummel & Baumgartner,
86 1991). Given that GRT-1 and GRT-2 wells penetrate geologic units similar to those in Soultz-sous-Forêts, information from
87 Soultz-sous-Forêts site can be used to better characterize the geological units through which the wells in Rittershoffen are
88 drilled (Aichholzer et al., 2016; Vidal et al., 2016). It can be used in particular for the strength and mechanical characteristics



89 of these geological units which are poorly characterized at Rittershoffen site since no coring was made during drilling
90 (Heap et al., 2017; Kushnir et al., 2018; Villeneuve et al., 2018). The World Stress Map (WSM) released in 2008 also
91 compiles the information available on the present-day stress field of the Earth's crust in the vicinity and gives an overview of
92 the values and results which can be expected in Rittershoffen (Cornet et al., 2007; Heidbach et al., 2010;
93 Rummel & Baumgartner, 1991; Valley & Evans, 2007a). The data collected from WSM are presented in Figure 1 and
94 indicate that an orientation of the maximum principal stress close to N169°E and a normal to strike slip faulting regime are
95 expected for our study area.

96 3. Rittershoffen well data

97 3.1 GRT-1 data

98 Several extensive logging programs accompanied the drilling of wells GRT-1 and GRT-2. One was conducted in December
99 2012 in the open-hole section of GRT-1, few days after drilling (Vidal et al., 2016). UBI acquisitions were carried out
100 (Luthi, 2001). Figure 2 (b) shows the amplitude image acquired in 2012 in GRT-1 and Fig. 2 (c) displays the radius of the
101 borehole computed from the double transit time image. The well logging also included caliper, spectral gamma ray and
102 gamma-gamma acquisitions that enable an estimation of rock alteration and bulk density. The injectivity measured during
103 the first hydraulic test between December 30th, 2012 and January 1st, 2013 showed a low injectivity (Baujard et al., 2017).
104 To enhance the injectivity, the hydraulic connectivity between the well and the natural fracture network has been increased
105 through a multi-step reservoir development strategy. First a thermal stimulation of the well has been performed in April
106 2013. A cold fluid (12°C) was injected at a maximum rate of 25 L.s⁻¹ with a maximum wellhead pressure of 2.8 MPa. The
107 total injected volume was 4230 m³. Second, a chemical stimulation followed in June 2013. Using open hole packers, a
108 glutamate-based biocide was injected in specific zones of the open hole section of GRT-1 (Baujard et al., 2017). Finally, a
109 hydraulic stimulation of the well has been performed in June 2013 with a large seismic monitoring at the surface
110 (Lengliné et al., 2017; Maurer et al., 2015). During these two last phases, a moderate volume injection, 4400 m³ were
111 injected in the open hole. The hydraulic stimulation lasted during 30h, with a major phase of stepwise flow rates from 10L.s⁻¹
112 to 80 L.s⁻¹ (Baujard et al., 2017). As a result, the injectivity was improved fivefold due to this thermal, chemical and
113 hydraulic (TCH) stimulation program. Two other borehole imaging programs were conducted in December 2013 shortly
114 after stimulation of the well and significantly later in June 2015. The amplitude and travel time (or radius) images used in the
115 analysis are shown respectively in Fig. 2 (e) and Fig. 2 (f) for the logging program of 2013 and in Fig. 2 (h) and Fig. 2 (i) for
116 the logging program of 2015.

117 This time lapse UBI dataset, whose characteristics are summarized in Table 1, provides the essential information for the
118 present study as it enables to identify evidences of irreversible deformation and failure (natural and induced fractures,
119 breakouts, fault zones, damage zones, etc) along the borehole wall. Vidal et al. (2016) analysed the images acquired in
120 GRT 1 and identified fractured zones impacted by the TCH stimulation, without assessing the stress state and its evolution.



121 Hehn et al. (2016), whose measurements are discussed later in section 9.2, analysed the orientation of DIFTs in GRT-1 in the
122 granitic basement but also in the upper sedimentary layers, investigating the orientation of the stress field with depth.
123 We identify wellbore wall failure and use these observations to characterise the stress state in the reservoir, including its
124 evolution in time. Wellhead pressure measurements of the hydraulic stimulation are also used to estimate a lower bound of
125 the minimum horizontal stress (Sh).

126 **3.2 GRT-2 data**

127 An extended logging program was also conducted in GRT-2, including repeated UBI borehole imaging (see Table 1). Figure
128 3(c) and 3(d) show respectively the amplitude image acquired in 2014, between 2404 m and 2412 m, and the radius image
129 acquired in 2015 between 2468 m and 2472 m, in GRT-2. No hydraulic stimulation was performed in this well since its
130 initial injectivity was sufficient (Baujard et al, 2017).

131 **4. Stress estimation methodology**

132 The approaches proposed by Zoback et al. (2003) and by Schmitt et al. (2012) are used to fully characterize the *in-situ* stress
133 field at the Rittershoffen geothermal project. In the following, the symbol S refers to the total stress when σ refers to the
134 effective stress (Jaeger & Cook, 2009). We suppose that one of the principal stresses of the *in-situ* stress tensor is vertical,
135 which is a common assumption. This hypothesis is justified by the first-order influence of gravity on the *in-situ* stress state,
136 although this assumption may not be valid locally. In the following, we denote the vertical principal stress, S_v . The
137 magnitude of the vertical stress S_v is obtained from the weight of the overburden. It is calculated by the integration of density
138 logs (see part 8.2). The two other principal stresses act horizontally: SH , the maximum horizontal stress and Sh , the
139 minimum horizontal stress. The magnitude of the minimum horizontal stress Sh is estimated from the wellhead pressure
140 measurements carried out during the hydraulic stimulation of GRT-1 and from the hydraulic tests performed in the reservoir
141 of Soultz-sous-Forêts (see part 8.3). The analysis of the borehole failures is evaluated using televiwer images data
142 (Zemanek et al., 1970; Zoback et al., 1985). The orientation and magnitude of SH is assessed using a failure condition at the
143 borehole wall.

144 **4.1 Wellbore stress concentration**

145 To express the stress concentration around the quasi-vertical borehole GRT-1 (maximum deviation is only of about 9°), we
146 assumed its shape to be a cylindrical hole, and used the well-known linear elastic solution, often referred to as the
147 Kirsch solution (Kirsch, 1898; Schmitt et al., 2012). For the deviated well GRT-2 where the plane strain approximation is
148 not valid anymore, we used a 3D solution taking into account its deviation (Schmitt et al. 2012). Note that we included in our
149 solution a thermal stress component that accounts for the thermal perturbation induced by the drilling process. This
150 component is detailed later in section 8.4. We used the formulation of the thermo-elastic stresses arising at a borehole given



151 by Voight & Stephens (1982), also recalled in Schmitt et al. (2012). We computed the effective stress at the borehole wall
 152 considering a hydrostatic pore pressure given by $Pp = \rho_f \cdot g \cdot z$, i.e. with the head level located at the surface. The fluid density
 153 ρ_f , is taken as $1000 \text{ kg}\cdot\text{m}^{-3}$ and the gravitational acceleration g , as $9.81 \text{ m}^2\cdot\text{s}^{-1}$. z is the vertical depth (TVD) in meter from
 154 ground surface.

155 4.2 Failure criterion

156 At the scale of the surrounding of borehole (a few decameters), we assume a linear elastic, homogeneous and isotropic rock
 157 behaviour prior to failure. When the maximum principal stress exceeds the compressive rock strength, rock fails in
 158 compression (Jaeger & Cook, 2009). Failure at the borehole wall is assessed using the elastic stress concentration solutions
 159 presented in part 4.1, combined with an adequate failure criterion. There is currently no consensus concerning the
 160 appropriate failure criteria to assess wellbore wall strength. Since, in the case where the pore pressure and the internal
 161 wellbore pressure are in equilibrium the radial effective stress at the borehole wall is equal to zero, a common assumption is
 162 to consider that the Uniaxial Compressive Strength (UCS) is a good estimate of wellbore strength (Barton et al., 1988;
 163 Zoback et al., 2003). Others suggest that the strength of borehole walls in low porosity brittle rocks could be less than the
 164 UCS, because the failure could be controlled by extensile strains (Barton & Shen, 2018; Walton et al., 2015) or fluid
 165 pressure penetration (Chang & Haimson, 2007). The presence of non-zero minimum principal stress and the strengthening
 166 effect of the intermediate principal stress however suggest that the borehole wall strength should be larger than UCS
 167 (Colmenares & Zoback, 2002; Haimson, 2006; Mogi, 1971). In view of this situation and because stress magnitudes
 168 evaluation differs according to the criterion used in the analysis, we compared the estimates obtained using three commonly
 169 used failure criteria in borehole breakouts analyses: 1) the Mohr-Coulomb criterion (Jaeger & Cook, 2009), 2) the Mogi-
 170 Coulomb criterion (Zimmerman & Al-Ajmi, 2006) and 3) a true triaxial version of the Hoek-Brown criteria (Zhang et al.,
 171 2010). The formulation of these criteria is given in the following equations (Eq. (1) to (3)) in the principal effective stress
 172 space $\sigma_1 - \sigma_3$ for the Mohr-Coulomb criterion and in octahedral shear vs. mean stress space $\tau_{oct} - \sigma_m$ for the Mogi-Coulomb
 173 and Hoek-Brown criteria:

$$174 \quad \text{Mohr-Coulomb: } \sigma_1 \geq C_0 + q \cdot \sigma_3 \quad (1)$$

$$175 \quad \text{Mogi-Coulomb: } \tau_{oct} \geq a + b \cdot \sigma_m \quad (2)$$

$$176 \quad \text{Hoek-Brown: } \frac{9}{2 \cdot C_0} \cdot \tau_{oct}^2 + \frac{3}{2\sqrt{2}} \cdot m_i \cdot \tau_{oct} - m_i \cdot \sigma_m \geq C_0 \quad (3)$$

177 Where C_0 is the uniaxial compressive strength and q is a material constant that can be related to the internal friction angle, φ ,
 178 through $q = \left(\frac{\pi}{4} + \frac{\varphi}{2}\right)$. The octahedral shear stress is given by $\tau_{oct} = \sqrt{(\sigma_1 + \sigma_2)^2 + (\sigma_2 + \sigma_3)^2 + (\sigma_3 + \sigma_1)^2}$ and the mean
 179 stress by $\sigma_m = \frac{\sigma_1 + \sigma_3}{2}$. The variables a and b in the Mogi-Coulomb criteria and m_i in the Hoek-Brown criteria are parameters
 180 that are related to the material friction and cohesion.



181 5. Strength estimation

182 Four simplified lithological categories have been used for the strength characterization of the rock at depth in the
183 Rittershoffen reservoir. All the Triassic sandstones have been grouped in a single category. The granitic section has been
184 separated in three categories according to the type and intensity of alteration. The simplified lithologic profile for GRT-1 and
185 GRT-2 wells are indicated in Table 2. Considering the methodology used here, the relevance and accuracy of the stress
186 characterization is highly conditioned by the values of the rock strength parameters and by the failure criterion chosen. In
187 Rittershoffen, the drilling was performed exclusively in destructive mode and no sample is available to measure rock moduli
188 and strength characteristics. Thereby, mechanical tests on core samples from the nearby Soultz-sous-Forêts site are used to
189 characterize the rock properties (Rummel, 1991; Valley & Evans, 2006). Indeed, boreholes of both sites penetrate the similar
190 lithological units and therefore using Soultz-sous-Forêts mechanical data for an application at the Rittershoffen site is
191 considered acceptable. At Soultz-sous-Forêts site, EPS-1 borehole was continuously cored from 930 to 2227 m
192 (Genter et al., 2010; Genter & Traineau, 1992, 1996) providing samples of the Sandstones in the Buntsandstein and in the
193 crystalline basement. Some cores have also been obtained in the borehole GPK-1 from various depth sections and were
194 analysed by Rummel (1992). For the Buntsandstein sandstones, because of the high variability of the rocks characteristics
195 within this same geological unit and because only very few tests were performed on these sandstones, we rather used typical
196 strength parameters (Hoek & Brown, 1997). The elastic and strength parameters used for our analyses are summarized in
197 Table 2. The variability range given for elastic parameters, cohesion and UCS reflect natural rock heterogeneities and depict
198 the variability in values encountered.

199 6. Images processing and borehole failure identification

200 Stress induced failures are identified and measured from acoustic borehole images. The confidence and accuracy of these
201 determinations depend on the quality of the images. In the following, we describe the original data as well as the processing
202 we applied to improve the quality and comparability of the images. We also explain how we measure borehole failure on
203 these images and the limitations associated with these measurements.

204 6.1 Quality of the acoustic televiewer images

205 Several artefacts can deteriorate the quality of acoustic image data (Lofts & Bourke, 1999). The images acquired in
206 Rittershoffen suffer from some of these limitations. The quality of the image depends of the tool specification, the
207 acquisition parameters and logging conditions. All acoustic images at Rittershoffen were acquired by Schlumberger with
208 their UBI (Ultrasonic Borehole Imager) tool. The tool and acquisition parameters were similar between each log, but not
209 identical. For example, the GRT-1 log in 2013 was acquired using a smaller acquisition head (see the changes in transducer
210 diameter detailed in Table 1. The acquisition resolution was the same for every log, i.e. 2° azimuthal resolution and 1 cm
211 depth sampling step.



212 The 2012 log of GRT-1 has the best quality image of the entire suite. The image suffers of signal loss artefact
213 (Lofts & Bourke, 1999) in some limited sections, most commonly related to the presence of breakouts or major fracture
214 zones (Fig. 3 (a)).

215 The 2013 log of GRT-1 is of comparable quality than the 2012 log and suffers also of some limited signal loss artefacts. The
216 major issue with the image of GRT-1 acquired in 2013 is that the orientation module was not included in the tool string and
217 thus the image cannot be oriented with magnetometer data as it is usually done for this type of data.

218 The 2015 log of GRT-1 generally suffers from signal loss issues, not only in areas with major fracture zones and breakouts.
219 In the lower part of the log, wood grain artefact (Lofts & Bourke, 1999) is also observable (see Fig. 3 (b)). This is
220 particularly developed below 2431 m MD.

221 The quality of data of logs from GRT-2 is generally worse than the ones of GRT-1. This is due to the deviation of GRT-2
222 that makes wireline logging more difficult. The 2014 log of GRT-2 suffers from stick-slip artefacts on its entire length
223 (Fig. 3 (c)). The 2015 log in GRT-2 does not show any sign of stick-slip but present an erroneous borehole radius record
224 leading to an incorrect borehole geometry evaluation (Fig. 3 (d)).

225 Despite these difficulties, the images collected in the GRT-1 borehole are of excellent quality. Signal loss is the main
226 problem and it prevents to measure the depth in the radial direction of the breakout in some zones. Given the extent of the
227 artefacts highlighted in GRT-2, the measurements of the breakout parameters in this borehole are much more uncertain.

228 6.2 Processing of the UBI images

229 Prior the use of the images for assessing borehole failure, the images went through the following pre-processing steps:

- 230 1) Transit time was converted to radius using the fluid velocity recorded during the probe trip down the borehole;
- 231 2) Images were filtered to reduce noise;
- 232 3) Digital image correlation was applied across the successive logs in order to correct the image misalignment both in
233 azimuth and depth.

234 The borehole radius was computed from the transit time following Luthi (2001):

$$235 \quad r = \frac{t_{tw} \cdot v_m}{2} + d \quad (4)$$

236 with t_{tw} the two-way travel time, v_m the acoustic wave velocity in the drilling mud, and d the logging tool radius. Images are
237 filtered using a selective despiking algorithm implemented in WellCad™ using a cut-off high level (75%) and a cut-off low
238 level (25%) in a 3x3 pixels window. The goal of this process is to replace outliers by cut-off values when the radius exceeds
239 the cut-off high or low level. Finally, digital image correlation was used to insure proper alignment of the UBI images. This
240 was required for the GRT-1 2013 image because this image was not oriented with a magnetometer/accelerometer tool. The
241 process was also applied to the 2015 GRT-1 data to facilitate comparison between images. For this purpose, we developed a
242 technique based on a Particle Image Velocimetry (PIV) method (Thielicke & Stamhuis, 2014) that relies on optical image
243 correlation but being applied to travel time UBI images. This image alignment process is illustrated in Fig. 4. Figure 4 (a)



244 shows as example the “correlation box” in the travel time UBI image of reference - i.e. 2012 in this case – and the
 245 corresponding one in the image to compare with - i.e. the image of 2013 – which it is shifted of a given displacement vector
 246 (dX, dY) within the “search box”. The cross-correlation function, which is a measure of the similarity between the
 247 thumbnails, is computed between the correlation boxes for each displacement vector (dX, dY) . Right panel of Figure 4 (a)
 248 shows a map of the cross-correlation function computed for every displacement vector in a given search box. The two-
 249 dimensional cross-correlation function is an operator acting on two intensity functions $s(X, Y)$ and $r(X, Y)$, defined as a norm
 250 of the colour levels at each position of each thumbnail. C_{sr} is defined at a position (X, Y) and for a shift (dX, dY) by Eq. (5):

251

$$252 \quad C_{sr}(dX, dY) = s(X, Y) \otimes r(X, Y) = \iint_{-\infty}^{+\infty} s(X, Y) r * (X - dX, Y - dY) dXdY \quad (5)$$

253

254

255 The position (dX, dY) within the “search box” with the highest cross correlation correspond to the best alignment
 256 (see Fig. 4 (a)). The operation is repeated along the image for each position of the search box. Importantly, the correlation
 257 box is taken with an anisotropic shape to account for the rigid rotation of the UBI tool and the linear property of the acoustic
 258 camera. The size of the correlation box is 180 x 20 pixels. This configuration is appropriate to identify principally the
 259 azimuthal offset while it is less sensitive to the depth mismatch. We investigated offset up to 180 pixels horizontally
 260 corresponding for our 2° resolution to a complete 360° rotation. We considered vertical offset of ± 10 pixels corresponding
 261 to offsets of about ± 10 cm. Figure 4 (b) gives an example of image realignment and shows the efficiency of the process.
 262 This correlation process allows to align finely the successive images and thus to study the borehole shape evolution with
 263 time more accurately.

264 6.3 Determination of the borehole failure

265 For GRT-1, the breakouts have been determined through a visual analysis of borehole sections computed every 20 cm from
 266 1926 m to 2568 m (MD) from the double transit time data. The borehole sections are computed by stacking (averaging using
 267 the median) the data collected every 1 cm over 20 cm borehole interval (with no overlap between two successive sections).
 268 The median is thus used because it is less sensitive to extreme values than the mean and thus is efficient at removing local
 269 noise from the data. Prior to determining breakout geometrical parameters, the actual borehole center is determined by
 270 adjusting the best fitted ellipse to the borehole section. This process corrects for eventual logging probe decentralisation. For
 271 each section presenting the characteristic elongated shape of breakouts due to stress induced failure, the azimuthal position
 272 of the edges and the center of each limb is determined by visual inspection. Figure 5 gives examples of such determination to
 273 depict the process. The breakout edges are defined as the location where the wellbore section departs from a quasi-circular
 274 section adjusted by the best fitted ellipse. As it can be seen in Figure 5, this typically spans an azimuthal range much broader
 275 than the low amplitude reflections visible as dark bands on the amplitude images and justifies the choice to use the double
 276 transit time data. The positions of the breakout edges are not easy to determine in a systematic and indisputable manner, and



277 a significant uncertainty is associated with these measurements. Related to this issue, it is not possible to determine on the
278 images what azimuthal range of the wellbore is enlarged by purely stress redistribution processes and what part is enlarged
279 subsequently by the effects of drill strings wear. These uncertainties about the physical process controlling the enlargement
280 of the breakout could limit the comparisons between the three successive logs acquired in GRT-1. Breakout measurements
281 were thus performed on all three images concomitantly and consistently. We controlled for example that within a tolerance
282 dictated by the uncertainties of the measurements, the width of breakouts only remains identical or increases: no decrease in
283 width is measured between successive logs.

284 Figure 2 (d), (g) and (j) summarize all the measurements of the breakout's geometry performed in GRT-1, for the images
285 acquired in 2012, 2013 and 2015. Black dots indicate the azimuth at which the radius of the breakout is maximum and red
286 bars link the azimuthal position of the breakout edges used to compute the width of the breakouts. Given the difficulty of
287 measuring breakouts as discussed previously (i.e. artefacts affecting the images, disputable positions of the breakout edges),
288 a confidence ranking has been established for each breakout. This confidence level is presented in Fig. 2 (k). From the
289 geometry of the breakouts, we compute the breakout widths which are obtained from the breakout edge azimuths. The
290 deepest point of the breakout is used to determine the enlargement radius. In some situations, signal loss issues prevent the
291 determination of the enlargement radius, as it is shown in Fig. 5 for the image of GRT-1 acquired in 2015. The measured
292 width (black dots, in degree) and enlargement radius (red dots, in mm) are determined from the GRT-1 data set acquired in
293 2012 and presented in Fig. 2 (l).

294 Drilling Induced Tension Fractures (DITFs) are also identified from the GRT-1 borehole images using the same procedure as
295 for the breakout determination. For example, clear DITFs are evidenced in the amplitude image from 2395 m to 2400 m in
296 GRT-1 and presented in Fig. 6. Green crosses show the azimuth of the DITFs that is measured in GRT-1 every 20 cm. Blue
297 dots in Fig. 2 (d), (g) and (j) summarize the azimuth of the DITFs measured in GRT-1, respectively in 2012, 2013 and 2015.
298 Given the poor quality of the double transit time images acquired in GRT-2, less focus has been given to the analysis of the
299 borehole failure in this well. The data set consists of the acquisitions made in 2014 after completion of the borehole and in
300 2015. The investigated depths vary from the 2014 to the 2015 dataset. It is from 1950 m (Vertical Depth – 2220 m MD)
301 down to 2125 m (TVD – 2440 m MD) in 2014 when it is down to 2160 m (TVD – 2480 m MD) in 2015. The well is
302 strongly deviated. The concentration of stresses within the borehole wall is expressed under the assumption of a constant
303 deviation of 37° and measurements carried out as a function of the True Vertical Depth, to be comparable with the results
304 obtained in GRT-1 which is considered as vertical. Borehole sections are computed every 50 cm. To this end, borehole
305 sections are stacked using the data collected every 1 cm over 50 cm borehole interval, all along the transit time image. As for
306 GRT-1, the actual borehole centre is determined by adjusting a best fitted ellipse to the borehole section. Breakouts are
307 analysed by visual analysis in a same manner as for GRT-1 data. The difficulties encountered with the identification of
308 breakout geometry are more pronounced for images acquired in GRT-2 as artefacts are more developed. The deviation of
309 this well results on pronounced stick-slip effects. For a more accurate comparison between the measurements carried out on



310 the images acquired in 2014 and 2015, measurements are performed for the two images concomitantly. No DITFs are
311 identified on the GRT-2 borehole images.

312 7. Analyses of temporal borehole failure evolution

313 The characterization of the stress tensor derived from the analysis of borehole failures typically relies on a single borehole
314 image data set. From this snapshot in time, stresses are estimated while information on the evolution of breakout shape in
315 time is not available. Interestingly, for the ECOGI project, the acquisition of three successive image logs allows to study this
316 evolution. Here, the time evolution of breakouts, referred as breakout development, is analysed to characterize the time
317 evolution of the borehole failure. A common hypothesis concerning borehole breakout evolution is that their width remains
318 stable and is controlled by the stress state around the well at the initial rupture time. Progressive failure is supposed to lead
319 however to breakout deepening until a stable profile is reached (Zoback et al., 2003).

320 An example of a time-lapse comparison of breakout shapes is presented in Fig. 7. Images of GRT-1 from 2012, 2013 and
321 2015 show a clear breakout at a depth of about 2126 m in the "couches de Trifels" in the Buntsandstein. Breakouts can
322 present three types of evolution:

- 323 1) They can develop along the well, corresponding to an increase in the vertical length of breakouts. We refer to this
324 process as *breakout extension*;
- 325 2) They can widen, corresponding to an apparent opening between the edges of the breakouts. We refer to this process
326 as *breakout widening*;
- 327 3) They can deepen, corresponding to an increase of the maximal radius of the breakout (or "depth" of the breakout)
328 measured in the borehole cross section at a given depth. We refer to this process as *breakout deepening*.

329 Figure 7 shows the evolution from 2012 to 2015 of the breakouts, at 2125.6 m. Failure did not occur in 2012 while breakouts
330 are visible in 2013 and 2015. When superposing the 2013/2015 borehole sections, no change in breakout shape is highlighted
331 for the west limb although a slight widening is visible on the east limb. Possible deepening of the east limb is occulted by
332 signal loss issues. The borehole section computed at 2126.2 m shows on the contrary, no modification of the breakout shape
333 from 2012 to 2015 in GRT-1.

334 Development of borehole failures depends also on the lithology. Breakout extension (longitudinal failure development) is
335 quite common in the Buntsandstein while it is very limited in the basement granites, which is highlighted in Fig. 8. The
336 evolution occurs exclusively between the 2012/2013 data set while no longitudinal extension occurs during 2013 and 2015.
337 In 2012, a total breakout length of 404 m is observed. It increases to 504 m in 2013 and then remains stable in 2015 with a
338 length of 506 m. There is no clear evolution of DITFs along the GRT-1 well despite the hydraulic and thermal stimulation
339 performed between 2012 and 2013.

340 Figure 9 shows an increase of breakout width. We first compare the data acquired in 2012 and in 2013. 73% of the change of
341 width is within an interval $-10^\circ / +10^\circ$, i.e. within our measurement uncertainty. For these breakouts no changes of width can



342 be highlighted within our level of uncertainty. However, for 27% of our data, we observe an increase of width larger than
343 10° . This is reflected by the long tail (with values higher than 10°) of the histogram computed from the width of breakouts
344 (see Fig. 9 (c)). The widening of these breakouts is undisputable. When comparing the data acquired in 2013 and in 2015,
345 very little changes are observed. Indeed, most of the measured changes remain below our uncertainty level of $\pm 10^\circ$ (red
346 histogram on Fig. 9 (c)).

347 The evolution of the maximum radial extension (breakout deepening) of the breakout measured in the borehole cross
348 sections is presented in Fig. 10. This parameter is more delicate to track because of signal loss issues (see for example
349 Fig. 3 (a)). In our analysis, we filtered out obvious incorrect depth measurements related to these artefacts, i.e. when the
350 computed radius from transit time image is clearly shorter than the drill bit radius. For both time intervals (2012-13 and
351 2013-15), the change in the depth of the breakout is symmetrically distributed around 0 mm and spans a variability of about
352 ± 15 mm. We interpret this distribution as an indication that if any deepening occurred, it remained within our uncertainty
353 level. Our data analysis does not enable to conclude in a general deepening of the breakouts.

354 8. Stress characterization

355 We propose in this section a complete stress characterization at different periods in both the GRT-1 and GRT-2 wells,
356 including a thermal history and thermal stress analyses and discuss the impact of breakout widening in time on stress
357 estimation. To that purpose, we first determine the orientation of the stress tensor. We then detail how we estimate the
358 minimum horizontal stress component Sh , the vertical stress component Sv and the thermal component. Finally, we propose
359 an estimation of the maximum horizontal stress component SH from the measurement of the width of breakouts.

360 8.1 Maximum horizontal stress SH orientation

361 The orientations of breakouts and DITFs are a direct measure of the principal stress directions in a plane perpendicular to the
362 well. As discussed previously, we assume that Sv is in-overall vertical which is a common hypothesis in such an approach
363 and is justified by the first-order effect of gravity on *in-situ* stresses. In GRT-1 which is considered as vertical, DITFs are
364 aligned with the direction of the maximum horizontal stress (SH) and breakouts are aligned with the direction of minimum
365 horizontal stress (Sh).

366 Figures 2 (d), (h) and (i) show the orientation of breakouts (black dots) and DITFs (blue dots) measured in GRT-1. The
367 measurements are compiled in Fig. 11 as circular histograms. We chose to only analyse data from the images acquired in
368 2012 and in 2015. Indeed, data acquired in 2013 were obtained without orientation since the device was not functioning
369 correctly and are reoriented with respect to the 2012 data. Subsequently, the measurements carried out in the 2013 image do
370 not bring additional constraints in terms of stress orientation.

371 In the Buntsandstein sediments, the failure orientation is stable and indicates that the principle stress SH is oriented
372 $N15^\circ \pm 19^\circ$ (one circular standard deviation). The same failure orientation persists in the upper section of the granite down to



373 about 2270 m. Below this depth borehole failure orientation is much more variable as it seems to be influenced by the
374 presence of major fault zones crossing the GRT-1 borehole at a depth of 2368 m (MD) (Vidal et al., 2016). Below 2420 m,
375 which is the deepest large structure visible on the GRT-1 borehole image, the failure orientation indicates that SH is oriented
376 $165^\circ \pm 14^\circ$. This is significantly different from the orientation in the sediments with a 30° counter-clockwise rotation. Such
377 differences in orientation with lithologies have already been noticed by Hehn et al. (2016) from the analysis of the
378 orientation of drilling induced fractures observed on borehole acoustic logs acquired in GRT-1. The orientation of SH
379 proposed by Hehn et al. (2016), i.e. globally N155°E in the basement and N20°E in the sedimentary layer, is consistent with
380 our measurements.

381 The geological study of the cuttings from the drilling of GRT-1 and GRT-2 enabled to determine the rock density profile in
382 both wells (Aichholzer et al., 2016). Thanks to this analysis, we estimate the mean density of each lithological layer. Table 3
383 shows the rock volumetric mass density as a function of the vertical depth (TVD). The magnitude of the vertical component
384 S_v at depth is computed accordingly by integrating the volumetric mass density profile and a linear regression is fitted to the
385 measurements obtained from surface. In the following, the vertical component S_v is computed from a linear trend expressed
386 as a function of vertical depth (TVD) z :

$$387 \quad S_v [MPa] = 0.024 \cdot z [m] - (0,83) \quad (6)$$

388

389 **8.3 Minimum horizontal stress Sh**

390 We take the first order assumption that the minimum horizontal stress Sh varies linearly with depth. Usually, the minimum
391 horizontal stress Sh is estimated at depth from hydrofracture tests, (i.e. Valley & Evans (2007)) but this was not done at
392 Rittershoffen site. If the data available for the ECOGI project limit our analysis of the minimum stress component, numerous
393 injection tests were conducted in Soultz-sous-Forêts. We present in Fig. 12 their main trends. The injection tests performed
394 in the deep wells (GPK-1, GPK-2 and GPK-3 or EPS-1) of Soultz-sous-Forêts (Cornet et al., 2007; Valley & Evans, 2007b)
395 give important constraints for the minimum horizontal stress Sh at the Rittershoffen site for large depths. In addition, the
396 study of Rummel & Baumgartner (1991) provides estimates at shallow depth. We compute the horizontal minimum stress Sh
397 as a function of the true vertical depth (TVD) z from the linear trend proposed by Cornet et al. (2007) for the site of Soultz-
398 sous-Forêts (Figure 15):

$$399 \quad Sh[MPa] = 0.015 \cdot z [m] - 7.3 \quad (7)$$

400

401 In order to check the applicability of the linear trend inferred from acquisitions in Soultz-sous-Forêts to the Rittershoffen
402 site, we estimated a lower bound of the minimum horizontal stress Sh at 1913 m in Rittershoffen from the measure of the
403 wellhead pressure during the hydraulic stimulation of GRT-1 (Baujard et al., 2017). Figure 13 shows that the variation of
404 wellhead pressure with the flow is slower during the high rate hydraulic stimulation (above $40 \text{ L}\cdot\text{s}^{-1}$) than during the low rate
405 hydraulic stimulation (below $40 \text{ L}\cdot\text{s}^{-1}$). This change in behavior is interpreted as the beginning of a pressure capping resulting



406 from fractures reactivation. Hydraulic stimulation typically increases pore pressure which reduces the effective stress until
407 pressure equals Sh in magnitude. In theory, an increase of pressure could activate new fractures which results in the capping
408 of the recorded pressure: in such a case, minimum horizontal stress is inferred at depth from the maximum pressure achieved
409 during such a test. Meanwhile, other processes (shearing of existing weak fractures for example) could possibly result in the
410 capping of pressure for lower pressure values. From Figure 13, we assume that wellhead pressure caps at 22.6 MPa at 1913m
411 (TMD) for a flow rate $80 \text{ L}\cdot\text{s}^{-1}$ (Fig. 12). It provides a lower bound to constrain the minimum horizontal stress Sh at depth,
412 which is compared to the Soultz-sous-Forêts trends in Fig. 13 and shows the consistency of the linear trend used in our
413 analysis.

414 8.4 Thermal stresses

415 The cooling of the well imposed during drilling, results in a thermal stress contribution. Accordingly, the characterization of
416 the stress tensor necessitates to include a thermal stress analysis which requires a good knowledge of the thermal history of
417 the well. We define the thermal contributions in the stress concentration at the borehole wall as: $\sigma^{\Delta T}_r$, $\sigma^{\Delta T}_z$ and
418 $\sigma^{\Delta T}_\theta$ respectively the radial, vertical and tangential components. The thermal stresses resulting from the temperature
419 difference, Δt , between the borehole wall and the so called ambient temperature, i.e. the initial temperature at that depth
420 before the drilling phase or the temperature at a significant distance from the borehole (not influenced by the borehole
421 perturbation), are expressed from Voight & Stephens (1982). These authors adapted the thermo-elastic solutions proposed by
422 Ritchie & Sakakura (1956) for a hollow cylinder to study the stress concentrations at the borehole wall due to the application
423 of a temperature difference. The radial component is null, and the tangential component is expressed as:

$$424 \sigma^{\Delta T}_\theta = \sigma^{\Delta T}_z = \alpha \cdot E \cdot \frac{\Delta T}{(1-\nu)} \quad (8)$$

425 where α is the thermal expansion, E , the Young modulus and ν , the Poisson ratio. Figure 14 (green curve) presents the
426 temperature log acquired in 2015 in GRT-1 (Baujard et al, 2017). It is plotted along with the temperature log acquired in
427 2013 (red curve). The comparison shows that temperature is close to be stable during that period in GRT-1. As a result, the
428 temperature log acquired in 2015 in GRT-1 is used as an estimate of the ambient temperature since it is considered as in
429 equilibrium with the reservoir. Temperature at the borehole walls at drilling completion is best estimated from the
430 temperature log acquired four days after drilling completion. The temperature log is presented in Fig. 14 (blue curve) and
431 the difference in temperature Δt computed from these logs is presented in the right panel of Fig. 14. Interestingly, these
432 temperature logs show a clear anomaly at 2360m where the wells are crossing the main fault zone associated to a major
433 permeable structure that controls two third of the total flow during flow tests (Baujard et al., 2017).
434



435 8.5 Maximum horizontal stress SH magnitude

436 The determination of the azimuthal position of the breakout's edges and of their width from the analysis of the UBI images
437 acquired in GRT-1 and GRT-2 enables to estimate the maximum horizontal stress SH , and to evaluate its evolution with
438 depth and time. Here, we present the results of our inversion, at multiple dates in GRT-1 and GRT-2.

439 In GRT-1, we obtain for each UBI log (in 2012, 2013 and 2015), three estimates of the magnitude of SH , according to the
440 failure criterion. Figure 15 shows estimates of the magnitude of SH . The maximum horizontal stress SH in GRT-1 is
441 presented for the 2013 UBI log as a function of the true vertical depth (TVD), along with the Sh and Sv obtained previously
442 (Eqs. (6) and (7)). The horizontal error bars are calculated from the uncertainty on the elastic parameters, on the Sh and Sv
443 estimates and on the measurements of the width of the breakouts. The uncertainty ΔSH is obtained by integration, taking into
444 account the uncertainty Δx_i on each variable x_i involved in the estimation of SH , i.e the strength parameters, the Sh and Sv
445 trends and the width of the breakouts:

$$446 \Delta f = \sum_i \left| \frac{\partial f}{\partial x_i} \right| \cdot \Delta x_i \quad (9)$$

447

448 Figure 15 shows that the SH magnitudes vary significantly with the failure criterion. In particular, it shows that the SH
449 stresses computed using a criterion that considers the strengthening effect of the intermediate principal stress (i.e. in Mogi-
450 Coulomb or Hoek Brown) are higher than those calculated from a criterion that considers only the minimum and maximum
451 principal stresses (i.e. in Mohr-Coulomb).

452 To choose the criterion that best describes the failure in the borehole, we use the approach proposed by Zoback et al. (2003)
453 to display the stress state estimates presented in Fig. 15 in the stress polygon whose circumference is defined by a purely
454 frictional, critically-stressed Earth crust. For this purpose, we suppose that crustal strength is limited by a Coulomb friction
455 criterion with a friction coefficient $\mu = 1$. We considered a depth of 2500 m to evaluate the vertical stress and assumed a
456 hydrostatic pore pressure. The possible stress states from 2013 UBI images, are shown in Fig. 16 in a normalized SH vs Sh
457 space. Because 2500 m is an upper boundary for the investigated depths in our study, the circumference of the polygon sets a
458 maximum value for the maximum and minimum horizontal stresses SH and Sh . The stresses are normalized by the vertical
459 stress magnitude Sv to facilitate the comparison. The maximum principal stresses SH measured using both our parametrized
460 Hoek-Brown and Mogi-Coulomb criteria (blue and black dots) exceed the polygon boundaries. With our selection of
461 parameters, the Mohr-Coulomb criterion was therefore retained as the most suitable for characterizing rock failure in our
462 study. The same conclusion was drawn by Valley & Evans (2015) in Basel.

463 For GRT-2, we calculated the SH magnitudes using only the Mohr-Coulomb criterion retained in the previous analysis.
464 GRT-2 is highly deviated and the well has been imaged in 2014 and 2015. The deviation is constant in the section of interest
465 (i.e. the open hole): 37° N355°E. SH stresses are shown as a function of the vertical depth (TVD) in Fig. 17 with the
466 according error bars and plotted along with the Sh and Sv trends in GRT-2.



467 The impact of breakout widening on stress estimation can be evaluated from our time-lapse characterization of the stress
468 tensor in GRT-1 and GRT-2. For GRT-2, Fig. 17 shows that SH magnitude changes are limited between 2014 and 2015,
469 given the uncertainty on the estimates. Figure 18 compares the SH stresses estimated using the Mohr-Coulomb criterion at
470 different dates in both GRT-1 and GRT-2 wells. The systematic shift observed between the estimates in both wells suggest
471 that the lower stresses estimated in the deviated well lead to a borehole wall stress concentration closer to the failure
472 condition than in the vertical well. Figure 18 evidences a time evolution of the SH stress estimates in GRT-1. Panel b.
473 quantifies the differences in SH stress between 2012 and 2015 in GRT-1 in a 1 MPa bins histogram. The confidence in the
474 time-evolution, is discussed in the next section considering the error on SH .

475 9. Discussion

476 The data set from the Rittershoffen geothermal project and our analyses allow us to discuss both the evolution over time and
477 with depth of the observed borehole failures. The impact of these evolutions on our ability to estimate stress magnitude from
478 borehole failure indicators is important.

479 9.1 Evolution of breakout geometry with time

480 Our analysis of the evolution of the breakouts geometry with time proves a development of breakouts along the well GRT-1
481 during the first year after drilling (Fig. 8). Indeed, we highlighted that sections without breakouts in 2012, four days after
482 drilling, present characteristic breakouts in 2013 and 2015, respectively one year and 2.5 years after drilling. We also
483 observe numerous lengths increases of the 2012 existing breakouts with time in particular in the Buntsandstein. The
484 difficulty is to link this evolution with time with a specific process: time-dependant rheology of the rock (i.e. creep) or the
485 effects of one of the stimulations, thermal, chemical or hydraulic. Moreover, the 2012 data were acquired at a period during
486 which the thermal perturbations due to the drilling operations were still present. The data they are compared with have been
487 collected in 2013 or 2015, after hydraulic, thermal and chemical stimulations of the well. As a result, the observed changes
488 could have taken place during the thermal equilibrium of borehole after drilling or during the simulations operations, i.e.
489 directly after drilling or later.

490 The conclusion brought by our time-evolution analysis of the breakout's geometry contradicts the usual assumption that
491 breakouts deepen (i.e. an increase in the maximum radius measured in the borehole cross sections) but do not widen (i.e. an
492 opening between the edges of the breakouts) with time (Zoback et al. 2003). However, the statistical approach applied in our
493 study along the open-hole of the well GRT-1 must be interpreted with caution. Even if we propose a systematic analysis of a
494 time-evolutive dataset, signal loss artefacts prevent an accurate measurement of borehole radius at some depths. It limits
495 locally our ability to reliably estimate the depth of the breakout, i.e. the extension of the breakout in the radial direction.
496 Given this limitation, we do not totally exclude that breakouts could have deepen with time. Our breakout width evaluation
497 is also affected by uncertainty: the deviation from the nominal cylindrical borehole geometry of the borehole adds



498 complexity to the measurements made considering the disputable positions of breakout edges. Meanwhile, we mitigated this
499 difficulty by proposing a systematic analysis of all dataset to ensure a more consistent measurement and by attributing an
500 uncertainty level on these values. Our study is thus more conclusive concerning this geometric parameter given that
501 measured changes exceed our uncertainty level.

502 The widening observed in our data set can be explained by the process of thermal stress dissipation. Indeed, the 30 to 35°C
503 of cooling observed at the time of the 2012 logging, are dissipated by the time of the 2013 logging (see Fig. 14). Assuming
504 thermo-elastic properties of the material, the thermal hoop stresses implied by the cooling reaches -17 to -20 MPa (Eq. (8)).
505 This will be sufficient to explain the change in breakout width without including additional time-dependent failure processes.

506 9.2 Evolution of breakout geometry with depth

507 The development of breakouts depends on the rock rheology and subsequently on the lithology. For our data set, breakouts
508 are more numerous and extended in the sedimentary cover than in the granitic basement (Fig. 2). Moreover, their
509 development is more pronounced in the sedimentary cover when they develop with time, vertically along the well (Fig. 8).
510 Both observations are consistent with the fact that the sediments have on average a lower strength compared to the granitic
511 rocks (Evans et al., 2009; Heap et al., 2019; Kushnir et al., 2018), i.e. conditions are closer to failure in the sediments.

512 Another important aspect of the variation of breakout geometry with depth is the evolution of their mean orientation. From
513 the combined measure of the azimuth of maximum radial extension of the breakouts (BOs) and of the azimuth of Drilling
514 Induced Tensile Fractures (DITFs), we analyse in Figure 11 the evolution with depth of the orientation of the maximum
515 principal stress SH . The measurements are repeated for the images acquired in GRT-1, in 2012 and in 2015. The consistency
516 between the orientation of our data between the 2012 and the 2015 data set (the 2013 data set was not oriented) builds
517 confidence in the reliability of these indicators.

518 Figure 11 suggests that the orientation measured in the granitic layers below 2420m in Rittershoffen is consistent with the
519 measurements carried out in the basement of Soultz-sous-Forêts (Valley & Evans, 2007b) and tends to reach the regional
520 orientation. The red line in Fig. 11 is a moving average of the orientation data. It is computed over a 20 m window in depth.
521 The measurement is carried out only if 50 individual measurements or more are present in the averaging window. It shows
522 that the orientation of the maximum principal stress SH varies in the studied section. Another important aspect of Figure 11
523 is the significant rotation of 30° from NNW to NNE highlighted between the bottom and the top of our analysed section.
524 Such rotation with depth has already been evidenced in the Upper Rhine graben area in the Basel geothermal boreholes
525 (Valley & Evans, 2009), in potash mines (Cornet & Röckel, 2012) and at the neighbouring geothermal site of Soultz-sous-
526 Forêts (Valley & Evans, 2007b). Hehn et al. (2016) have also evidenced local stress rotations in the sedimentary section of
527 GRT-1 up to the upper Triassic (Keuper) from the analyses of DITFs. The orientation measured here above the limit set
528 close to 2400m MD (Fig. 11), is also consistent with the measurements of Hehn et al. (2016). They interpreted these
529 variations to be related to mechanical contrasts between stiffer and softer rock layers. The particularity of the measurements
530 proposed in Fig. 11 is that the orientation of the maximum principal stress SH deviates from the regional trend within the



531 granitic basement, while the measurement in the upper basement aligns with the orientation of the sedimentary cover
532 (Fig. 11). The presence of a major fault crossing the GRT-1 borehole at a depth of 2368 m MD (Vidal et al., 2016) could be
533 the explanation of this rotation. The location of the observed stress rotation, i.e. in the basement and around 50m above the
534 major fault zone, doesn't assume that it is related here to the stiffness contrast or decoupling between the sedimentary cover
535 and the underlying basement as typically assumed, but rather to the presence of a neighbouring major fault zone.
536 Considering a high dipping fault geometry for this fault zone, it suggests that the geothermal well tangents the fault zone
537 explaining why breakouts are observed below but also above the major drain of the fault zone located at 2368 m (Fig 11).
538 Moreover, it was clearly demonstrated based on continuous granite core analyses at Soultz, that fault zone could have a
539 significant thickness due to the presence of a damaged zone characterized by an intense hydrothermal alteration
540 (Genter et al., 2010). Therefore, the absence of breakouts visible in the altered granitic section located just above the main
541 fault drain and the anticipated rotation of the stress field at some distance in the hanging wall and the footwall of the fault
542 zone confirm its major mechanical influence.

543 **9.3 Evaluation of stress magnitude from breakout width**

544 Our study shows the sensitivity to the failure criterion. Our analyses suggest that the Mogi-Coulomb and Hoek-Brown
545 criteria tend to overestimate borehole wall strength because they lead to stress estimates that violate frictional strength limit
546 of the crust (Fig. 16) while the Mohr-Coulomb strength model leads to acceptable results. This conclusion is however
547 dependent of the detailed parameterization of the failure criterion which is in Rittershoffen supported by sparse data. The
548 rock strength is among the main parameters that impact the stress magnitude assessment. At the Rittershoffen project, we
549 have no access to direct strength measurements since no cores were collected. We rely on measurement at the neighbouring
550 Soultz-sous-Forêts site where cores are available. However, even at Soultz-sous-Forêts, a systematic characterization of the
551 rock strength of the various lithologies is not achievable, particularly for the sediments.

552 In addition to the uncertainty on the strength parameterization, the uncertainty on width determination and the evolution of
553 width with time further impact the stress estimation. In the case of the GRT-1, significant changes occur between the 2012
554 data set (prior to reservoir stimulation operations) and the 2013-15 data sets (after stimulation). Panel (b) of Figure 18 shows
555 that the changes in the SH stresses between 2012 and 2015 in GRT-1 are larger than our measurement uncertainty for 15% of
556 the measurements and are showing principally stress increases. This change can be fully explained by the thermal
557 equilibration of the well. The uncertainty on our data doesn't allow to relate stress changes to the reservoir stimulation
558 operations.

559 **9.4 Stresses magnitude evolution with depth**

560 Stresses estimated in GRT-1 and GRT-2 suggest that SH is generally close to the vertical principal stresses S_v consistently
561 with a transitional regime between both strike-slip regime and normal faulting regime (Anderson, 1951). This is consistent
562 with the stress characterization of the neighbouring site of Soultz-sous-Forêts, where measurements have highlighted a



563 normal faulting regime in the top granitic layers evolving into a strike slip regime more in depth. The uncertainty about our
564 measurements and about the strength parameterization does not allow, however, for a decision on the faulting regime and its
565 evolution with depth in Rittershoffen. A step in *SH* magnitude is visible on our estimate in Fig. 18 at large depth (below
566 2250m). This step occurs at the interface sediment basement and could be explained by the effect of stiffness contrast
567 between lithologies (Corkum et al., 2018).

568 10. Conclusion

569 Thanks to the repeated UBI logging of the geothermal wells GRT-1 and GRT-2 in Rittershoffen (France), this study focuses
570 on the analysis of the evolution with time and depth of the borehole breakouts. The following conclusions are drawn:

- 571 (i) Clear evidences of time evolution of the breakout exist in particular in the sedimentary cover.
- 572 (ii) The evolution in time of the vertical length and the horizontal width of the breakouts are measured
573 benefiting from the development of a UBI image correlation technique It is discussed in the limit of the
574 estimated uncertainties. The vertical length of the breakouts is shown to increase with time. No variation in
575 the depth of the breakouts in the radial direction was observed within the limit of the uncertainty of our
576 analysis. However, width increases beyond the uncertainty of our determination were highlighted. This
577 contradict the common assumption that breakouts do not widen but only deepen until the borehole reach a
578 new stable state (Zoback et al. 2003);
- 579 (iii) The changes in breakout width occur between datasets collected prior and after reservoir stimulation.
580 However, the most likely effect on breakout width is the thermal equilibration of the wellbore and our data
581 do not evidence stress changes result from reservoir stimulation;

582 In addition to this analysis, the study of the geometry of borehole failures in both wells leads to propose a characterization of
583 the *in-situ* stress tensor at depths including the orientation and the magnitude of the three principal stresses. This detailed
584 stress state analysis includes the estimation of thermal stresses. A Mohr-Coulomb criterion is retained here to estimate the
585 principal stresses magnitude as it is in our parametrization, the most consistent with a frictional strength limit in the crust.
586 The strength parameterization is however uncertain due to the lack of mechanical testing on the Rittershoffen reservoir
587 rocks. Given the uncertainties, we propose the following careful interpretation of our measurements:

- 588 (i) Our analyses of the breakout geometry variation with depth suggest a change in mean orientation, with a 30°
589 rotation from NNW to NNE highlighted between the bottom and the top of our analysed section. This
590 observation is robust and independent of the strength parameterisation. The rotation does not occur at the
591 sediment-basement interface but is related to a high steeply dipping major fault zone crossing the GRT-1
592 borehole at a depth of 2368 m (Vidal et al., 2016).



593 (ii) Our results suggest also a step in horizontal stress magnitude at the sediment to basement transition that would
594 be consistent with stiffness contrast between these two lithologies. However, such step is determined by the
595 choice of the failure criterion and its parameterization which is uncertain at Rittershoffen.

596 (iii) SH is generally slightly larger than the vertical principal stresses S_v consistently with a strike-slip to normal
597 faulting transitional regime. This is consistent with stress characterization at the neighbour site of Soultz-sous-
598 Forêts (Cornet et al., 2007; Klee & Rummel, 1993; Valley & Evans, 2007b)

599

600 The Rittershoffen borehole imaging dataset is unique by the fact that repeating logging allowed to study the temporal
601 evolution of borehole breakouts and the possible stress changes induced by reservoir stimulation. Our results change the
602 common view that breakouts mostly deepen but do not widen. Further work is however required to reduce the uncertainties
603 related to stress magnitude estimates from borehole breakouts and to be able to quantify stress changes induced by reservoir
604 stimulation.

605



606 **Availability of data and materials**

607 Due to the industrial property of the borehole datasets, raw data would remain confidential and would not be shared.

608 **Competing interests**

609 The authors declare no competing financial interest.

610 **Funding**

611 This work has been published under the framework of the LABEX ANR- 11-LABX-0050-G-EAU- THERMIE-PROFONDE
612 and benefits from a funding from the state managed by the French National Research Agency (ANR) as part of the
613 ‘Investments for the Future’ program. It has also been funded by the EU projects DESTRESS (EU H2020 research and
614 innovation program, grant agreement No 691728).

615 **Acknowledgments**

616 We thank ÉS-Géothermie, subsidiary company of Électricité de Strasbourg (ÉS), for support and allowing us the use of
617 borehole data on wells GRT-1 and GRT-2 of the Rittershoffen ECOGI project. A part of this work was conducted in the
618 framework of the EGS Alsace project, which was co-founded by ADEME.

619 We would like to thank the Swiss Competence Center for Energy Research–Supply of Electricity (SCCER-SoE) for support
620 of the study. The present work has been done under the framework of the LABEX ANR-11-LABX-0050-G-EAU-
621 THERMIE-PROFONDE and benefits from a state funding managed by the French National Research Agency (ANR) as part
622 of the “Investments for the Future” program.

623



624 **11. References**

- 625 Aichholzer, C., Düringer, P., Orciani, S., & Genter, A.: New stratigraphic interpretation of the Soultz-sous-Forêts 30-year-
626 old geothermal wells calibrated on the recent one from Rittershoffen (Upper Rhine Graben, France). *Geothermal*
627 *Energy*, 4(1), <https://doi.org/10.1186/s40517-016-0055-7>, 2016.
- 628 Anderson, E. M.: *The dynamics of faulting*, 1951.
- 629 Barton, C.A., & Shen, B.: Extension Strain and Rock Strength Limits for Deep Tunnels, Cliffs, Mountain Walls and the
630 Highest Mountains. *Rock Mechanics and Rock Engineering*, 51(12), 3945–3962. [https://doi.org/10.1007/s00603-](https://doi.org/10.1007/s00603-018-1558-2)
631 018-1558-2, 2018.
- 632 Barton, C.A., Zoback, M. D., & Burns, K. L.: Insitu stress orientation and magnitude at the Fenton geothermal site,
633 determined from breakouts analysis, *Geophysical Research Letters*, 1951.
- 634 Baujard, C., Genter, A., Graff, J.J, Maurer, V., & Dalmais, E.: ECOGI, a new deep EGS project in Alsace, Rhine Graben,
635 France. In *World geothermal Congress*. Melbourne, Australia. 2015.
- 636 Baujard, C., Genter, A., Dalmais, E., Maurer V., Hehn, R. Rosillette, R., et al.: Hydrothermal characterization of wells GRT-
637 1 and GRT-2 in Rittershoffen, France: Implications on the understanding of natural flow systems in the rhine
638 graben. *Geothermics*, 65, 255–268. <https://doi.org/10.1016/j.geothermics.2016.11.001>, 2017.
- 639 Chang, C., & Haimson, B.: Effect of fluid pressure on rock compressive failure in a nearly impermeable crystalline rock:
640 Implication on mechanism of borehole breakouts. *Engineering Geology*, 89(3–4), 230–242.
641 <https://doi.org/10.1016/j.enggeo.2006.10.006>, 2007.
- 642 Colmenares, L., & Zoback, M.: A statistical evaluation of intact rock failure criteria constrained by polyaxial test data for
643 five different rocks. *International Journal of Rock Mechanics and Mining Sciences*, 39(6), 695–729.
644 [https://doi.org/10.1016/S1365-1609\(02\)00048-5](https://doi.org/10.1016/S1365-1609(02)00048-5), 2002.
- 645 Corkum, A.G., Damjanac, B., & Lam, T.: Variation of horizontal in situ stress with depth for long-term performance
646 evaluation of the Deep Geological Repository project access shaft. *International Journal of Rock Mechanics and*
647 *Mining Sciences*, 107, 75–85. <https://doi.org/10.1016/j.ijrmms.2018.04.035>, 2018.
- 648 Cornet, F., & Röckel, T.: Vertical stress profiles and the significance of “stress decoupling.” *Tectonophysics*, 581, 193–205.



- 649 <https://doi.org/10.1016/j.tecto.2012.01.020>, 2012.
- 650 Cornet, F., Bérard, T., & Bourouis, S.: How close to failure is a granite rock mass at a 5km depth? *International Journal of*
651 *Rock Mechanics and Mining Sciences*, 44(1), 47–66. <https://doi.org/10.1016/j.ijrmms.2006.04.008>, 2007.
- 652 Cornet, F. H.: Elements of crustal geomechanics. *Cambridge University Press*, 2015.
- 653 Dezayes, C., Gentier, S., & Genter, A.: *Deep geothermal energy in western Europe: the Soultz project*. BRGM/RP-54227-
654 FR, 48p., 2005
- 655 Dorbath, L., Evans, K., Cuenot, N., Valley, B., Charléty, J., & Frogneux, M.: The stress field at Soultz-sous-Forêts from
656 focal mechanisms of induced seismic events: Cases of the wells GPK2 and GPK3. *Comptes Rendus Geoscience*,
657 342(7–8), 600–606. <https://doi.org/10.1016/j.crte.2009.12.003>, 2010.
- 658 Evans, K., Valley, B., Häring, M., Hopkirk, R., Baujard, C., Kohl, T., et al. : *Studies and support for the EGS reservoirs at*
659 *Soultz-sous-Forêts*. Technical report, Centre for Geothermal Research–CREGE, c/o CHYN, University of
660 Neuchâtel, 2009.
- 661 Genter, A., Traineau, H. Borehole EPS-1, Alsace, France: preliminary geological results from granite core analyses for Hot
662 Dry Rock research. *International Journal of Rock Mechanics and Mining Sciences & Geomechanics Abstracts*,
663 30(3), A171. [https://doi.org/10.1016/0148-9062\(93\)92984-X](https://doi.org/10.1016/0148-9062(93)92984-X), 1992.
- 664 Genter, A., & Traineau, H. Analysis of macroscopic fractures in granite in the HDR geothermal well EPS-1, Soultz-sous-
665 Forêts, France. *Journal of Volcanology and Geothermal Research*, 72(1–2), 121–141. [https://doi.org/10.1016/0377-0273\(95\)00070-4](https://doi.org/10.1016/0377-0273(95)00070-4), 1996.
- 666
- 667 Genter, A., Evans, K., Cuenot, N., Fritsch, D., & Sanjuan, B. Contribution of the exploration of deep crystalline fractured
668 reservoir of Soultz to the knowledge of enhanced geothermal systems (EGS). *Comptes Rendus Geoscience*, 342(7–
669 8), 502–516. <https://doi.org/10.1016/j.crte.2010.01.006>, 2010.
- 670 Haimson, B.: True Triaxial Stresses and the Brittle Fracture of Rock. *Pure and Applied Geophysics*, 163(5–6), 1101–1130.
671 <https://doi.org/10.1007/s00024-006-0065-7>, 2006
- 672 Heap, M. J., Kushnir, A. R. L., Gilg, H. A., Wadsworth, F. B., Reuschlé, T., & Baud, P.: Microstructural and petrophysical
673 properties of the Permo-Triassic sandstones (Buntsandstein) from the Soultz-sous-Forêts geothermal site (France).



- 674 *Geothermal Energy*, 5(1). <https://doi.org/10.1186/s40517-017-0085-9>, 2017.
- 675 Heap, M. J., Villeneuve, M., Kushnir, A. R. L., Farquharson, J. I., Baud, P., & Reuschlé, T.: Rock mass strength and elastic
676 modulus of the Buntsandstein: An important lithostratigraphic unit for geothermal exploitation in the Upper Rhine
677 Graben. *Geothermics*, 77, 236–256. <https://doi.org/10.1016/j.geothermics.2018.10.003>, 2019.
- 678 Hehn, R., Genter, A., Vidal, J., & Baujard, C.: Stress field rotation in the EGS well GRT-1 (Rittershoffen, France), 2016.
- 679 Heidbach, O., Tingay, M., Barth, A., Reinecker, J., Kurfeß, D., & Müller, B.: Global crustal stress pattern based on the
680 World Stress Map database release 2008. *Tectonophysics*, 482(1–4), 3–
681 15. <https://doi.org/10.1016/j.tecto.2009.07.023>, 2010.
- 682 Hoek, E., & Brown, E. T.: Practical estimates of rock mass strength. *International Journal of Rock Mechanics and Mining
683 Sciences*, 34(8), 1165–1186. [https://doi.org/10.1016/S1365-1609\(97\)80069-X](https://doi.org/10.1016/S1365-1609(97)80069-X), 1997.
- 684 Huenges, E., & Ledru, P.: *Geothermal energy systems: exploration, development, and utilization*. John Wiley & Sons, 2011.
- 685 Jaeger, J. C., & Cook, N.G.W.: *Fundamentals of rock mechanics* (3d ed). London : New York: Chapman and Hall ;
686 distributed in U.S. by Halsted Press, 2009.
- 687 Kirsch, C.: Die Theorie der Elastizität und die Bedürfnisse der Festigkeitslehre. *Zeitschrift Des Vereines Deutscher
688 Ingenieure*, 42, 797–807, 1898.
- 689 Klee, G., & Rummel, F.: Hydrofrac stress data for the European HDR research project test site Soultz-Sous-Forets.
690 *International Journal of Rock Mechanics and Mining Sciences & Geomechanics Abstracts*, 30(7), 973–976.
691 [https://doi.org/10.1016/0148-9062\(93\)90054-H](https://doi.org/10.1016/0148-9062(93)90054-H), 1993.
- 692 Kushnir, A. R. L., Heap, M. J., Baud, P., Gilg, H. A., Reuschlé, T., Lerouge, C., et al.: Characterizing the physical properties
693 of rocks from the Paleozoic to Permo-Triassic transition in the Upper Rhine Graben. *Geothermal Energy*, 6(1).
694 <https://doi.org/10.1186/s40517-018-0103-6>, 2018.
- 695 Lengliné, O., Boubacar, M., & Schmittbuhl, J.: Seismicity related to the hydraulic stimulation of GRT1, Rittershoffen,
696 France. *Geophysical Journal International*, ggw490. <https://doi.org/10.1093/gji/ggw490>, 2017
- 697 Lofts, J. C., & Bourke, L. T.: The recognition of artefacts from acoustic and resistivity borehole imaging devices. *Geological
698 Society, London, Special Publications*, 159(1), 59–76. <https://doi.org/10.1144/GSL.SP.1999.159.01.03>, 1999.



- 699 Luthi, S. M.: Geological Well Logs: Use in Reservoir Modeling. *Log Interpretation, II.*, 2001.
- 700 Maurer, V., Cuenot, N., Gaucher, E., Grunberg, M., Vergne, J., Wodling, H., et al. : Seismic Monitoring of the Rittershoffen
701 EGS Project (Alsace, France), 2015.
- 702 Mogi, K.: Fracture and flow of rocks under high triaxial compression. *Journal of Geophysical Research*, 76(5), 1255–1269.
703 <https://doi.org/10.1029/JB076i005p01255>, 1971.
- 704 Ritchie, R. H., & Sakakura, A. Y.: Asymptotic Expansions of Solutions of the Heat Conduction Equation in Internally
705 Bounded Cylindrical Geometry. *Journal of Applied Physics*, 27(12), 1453–1459. <https://doi.org/10.1063/1.1722288>,
706 1956.
- 707 Rummel, F.: Physical Properties of the rock in the granitic section of borehole GPK1, Soultz-Sous-Forêts. *Geotherm Sci*
708 *Tech*, 3, 199–216, 1991.
- 709 Rummel, F., & Baumgartner, F.: Hydraulic fracturing stress measurements in GPK-1 borehole, Soultz-Sous-Forêts.
710 *Géotherm Sci Tech*, 119–148, 1991.
- 711 Schmitt, D. R., Currie, C. A., & Zhang, L.: Crustal stress determination from boreholes and rock cores: Fundamental
712 principles. *Tectonophysics*, 580, 1–26. <https://doi.org/10.1016/j.tecto.2012.08.029>, 2012.
- 713 Thielicke, W., & Stamhuis, E. J. : PIVlab – Towards User-friendly, Affordable and Accurate Digital Particle Image
714 Velocimetry in MATLAB. *Journal of Open Research Software*, 2. <https://doi.org/10.5334/jors.bl>, 2014.
- 715 Valley, B., & Evans, K. F.: Strength and elastic properties of the Soultz granite. In *Proceedings of the Annual Scientific*
716 *Meeting of the Soultz Project, Soultz-sous-Forêts, France*, 2006.
- 717 Valley, B., & Evans, K. F.: Estimation of the Stress Magnitudes in Basel Enhanced Geothermal System, 2007a.
- 718 Valley, B., & Evans, K. F.: Stress State at Soultz-Sous-Forêts to 5 Km Depth from Wellbore Failure and Hydraulic
719 Observations, 2007b.
- 720 Vidal, J., Genter, A., & Schmittbuhl, J.: Pre- and post-stimulation characterization of geothermal well GRT-1, Rittershoffen,
721 France: insights from acoustic image logs of hard fractured rock. *Geophysical Journal International*, 206(2), 845–
722 860. <https://doi.org/10.1093/gji/ggw181>, 2016.
- 723 Villeneuve, M. C., Heap, M. J., Kushnir, A. R. L., Qin, T., Baud, P., Zhou, G., & Xu, T.: Estimating in situ rock mass



- 724 strength and elastic modulus of granite from the Soultz-sous-Forêts geothermal reservoir (France). *Geothermal*
725 *Energy*, 6(1), 11. <https://doi.org/10.1186/s40517-018-0096-1>, 2018.
- 726 Voight, B., & Stephens, G.: Hydraulic fracturing theory for condition of thermal stress, *Vol.19*, pp.279-284, 1982.
- 727 Walton, G., Kalenchuk, K. S., Hume, C. D., & Diederichs, M. S.: Borehole Breakout Analysis to Determine the In-Situ
728 Stress State in Hard Rock. In *ARMA-2015-553* (p. 9). ARMA: American Rock Mechanics Association, 2015.
- 729 Zemanek, J., Glenn, E. E., Norton, L. J., & Caldwell, R. L.: Formation evaluation by inspection with the borehole televiewer.
730 *Geophysics*, 35(2), 254–269. <https://doi.org/10.1190/1.1440089>, 1970.
- 731 Zhang, L., Cao, P., & Radha, K. C.: Evaluation of rock strength criteria for wellbore stability analysis. *International Journal*
732 *of Rock Mechanics and Mining Sciences*, 47(8), 1304–1316. <https://doi.org/10.1016/j.ijrmms.2010.09.001>, 2010.
- 733 Zimmerman, R.W., & Al-Ajmi, A. M.: Stability Analysis of Deviated Boreholes using the Mogi-Coulomb Failure Criterion,
734 with Applications to some North Sea and Indonesian Reservoirs. Society of Petroleum Engineers.
735 <https://doi.org/10.2118/104035-MS>, 2006.
- 736 Zoback, M.D., Moos, D. B., & Mastin: Well Bore Breakouts and in Situ Stress.pdf. *US Geological Survey*, 1985.
- 737 Zoback, M.D., Barton, C.A., Brudy, M., Castillo, D. A., Finkbeiner, T., Grollmund, B. R., et al.: Determination of stress
738 orientation and magnitude in deep wells. *International Journal of Rock Mechanics and Mining Sciences*, 40(7–8),
739 1049–1076. <https://doi.org/10.1016/j.ijrmms.2003.07.001>, 2003.

740

741

742

743

744

745

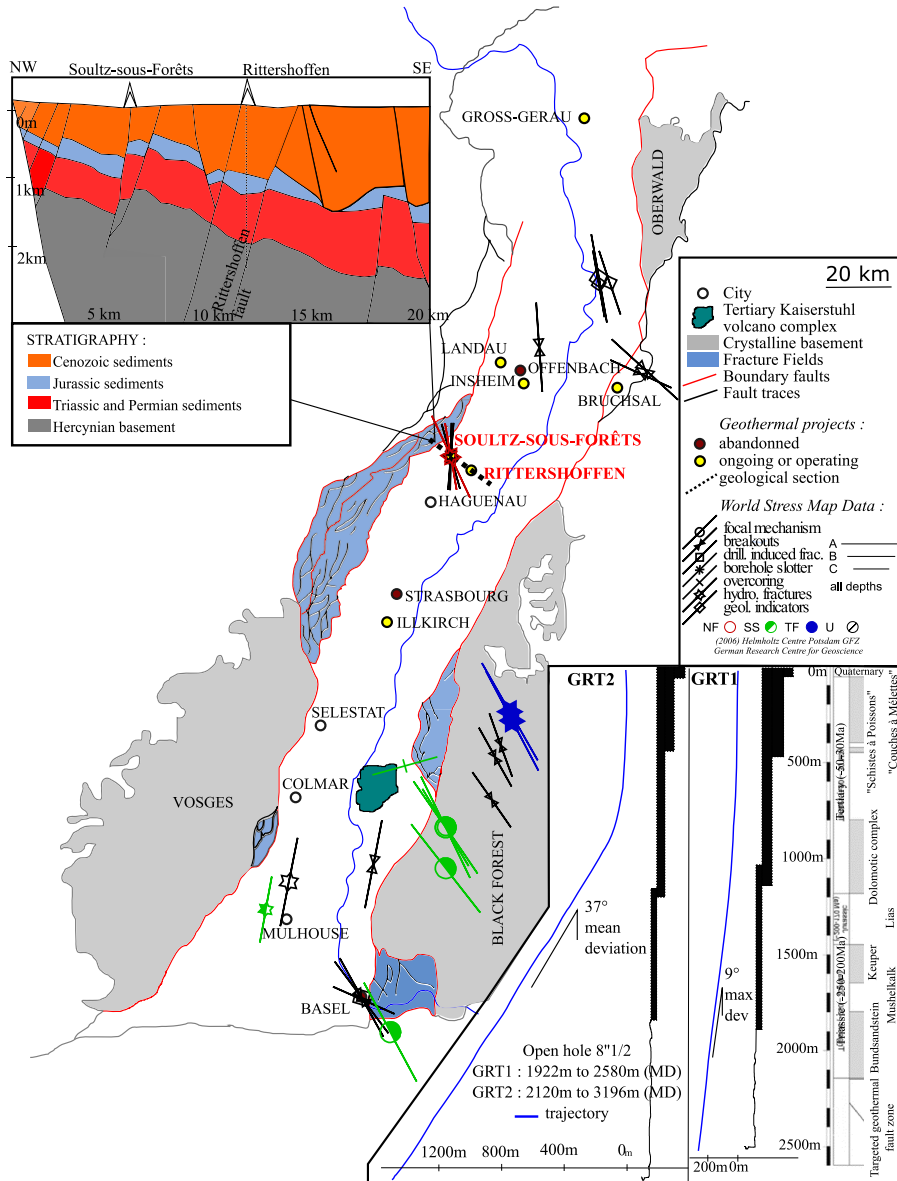




Figure 1: Geological and structural map of the main of the Upper Rhine Graben with the location of the Rittershoffen and Soultz-sous-Forêts sites. The map shows also the location and status of other neighbouring deep geothermal projects. Stress data from World stress map database (Heidbach et al., 2010) are included. Upper left insert shows a geological section highlighting the main units crossed by the wells in Rittershoffen and Soultz-sous-Forêts (Aichholzer et al., 2016; Baujard et al., 2017). Lower right insert is a sketch of wells GRT-1 and GRT-2 drilled in Rittershoffen, including their geometry, depths and crossed lithology (after Baujard et al. (2015, 2017)).

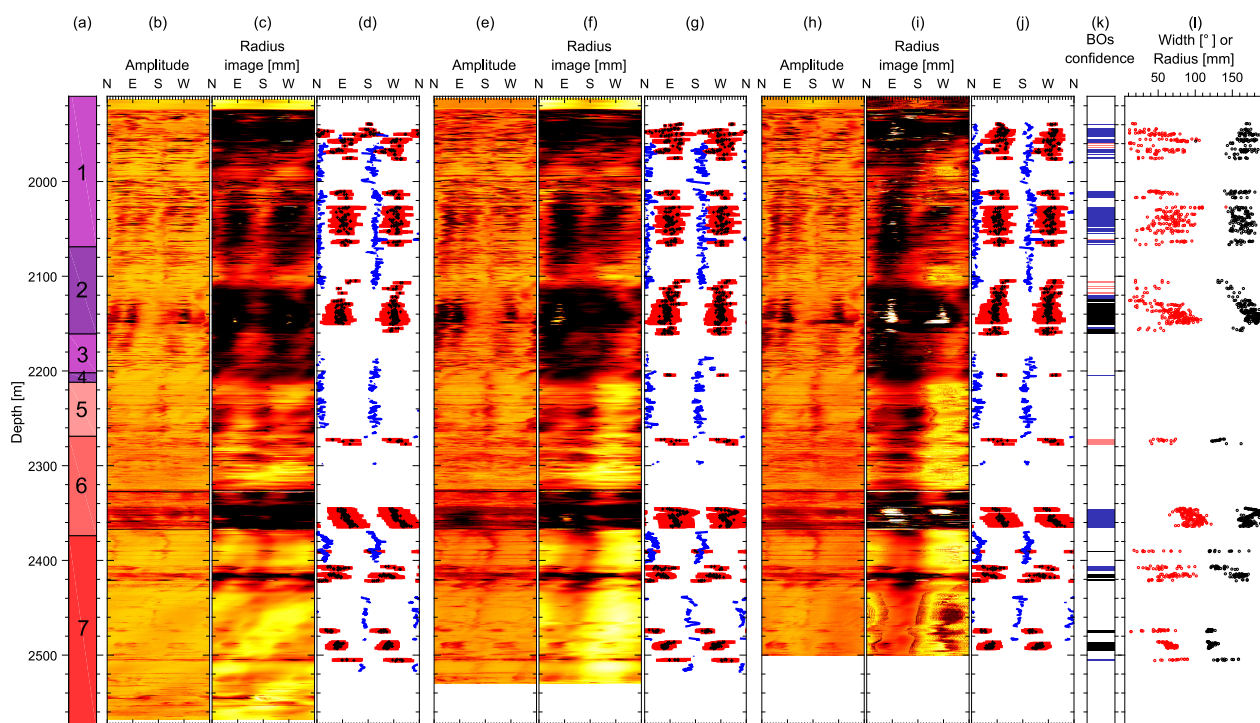




Figure 2: Synthesis of the data used in this analysis of the borehole GRT-1. (a) simplified lithologic column. (1) stands for “couches de Rehberg”, (2) for “Couches de Trifels”, (3) for Annweiler sandstone, (4) for Permian layers older than Annweiler sandstone, (5) for rubefied granite, (6) for hydrothermally altered granite and (7) for low altered granite. The UBI images are presented, as well as the data picked from the visual analysis of the double transit time image for the dataset of 2012 (panel b. - c. - d.), 2013 (e. - f. - g.), and 2015 (h. - i. - j.) collected in GRT-1. The radius of the borehole computed from the double transit time image is displayed in panels b. - e. and h. In panels d. - g. and j., blue dots represent the azimuth of the Drilling Induced Tension Fractures (DITFs), black dots represent the azimuth of the maximal radial depth of the breakouts and red bars represent the extension between the edges of the breakouts. Panel l. summarizes the width (black dots, in °) and the enlargement radius (red dots, in mm) measured in the 2012, 2013 and 2015 images and panel k. informs about the breakouts (BOs) confidence level applied to these results.

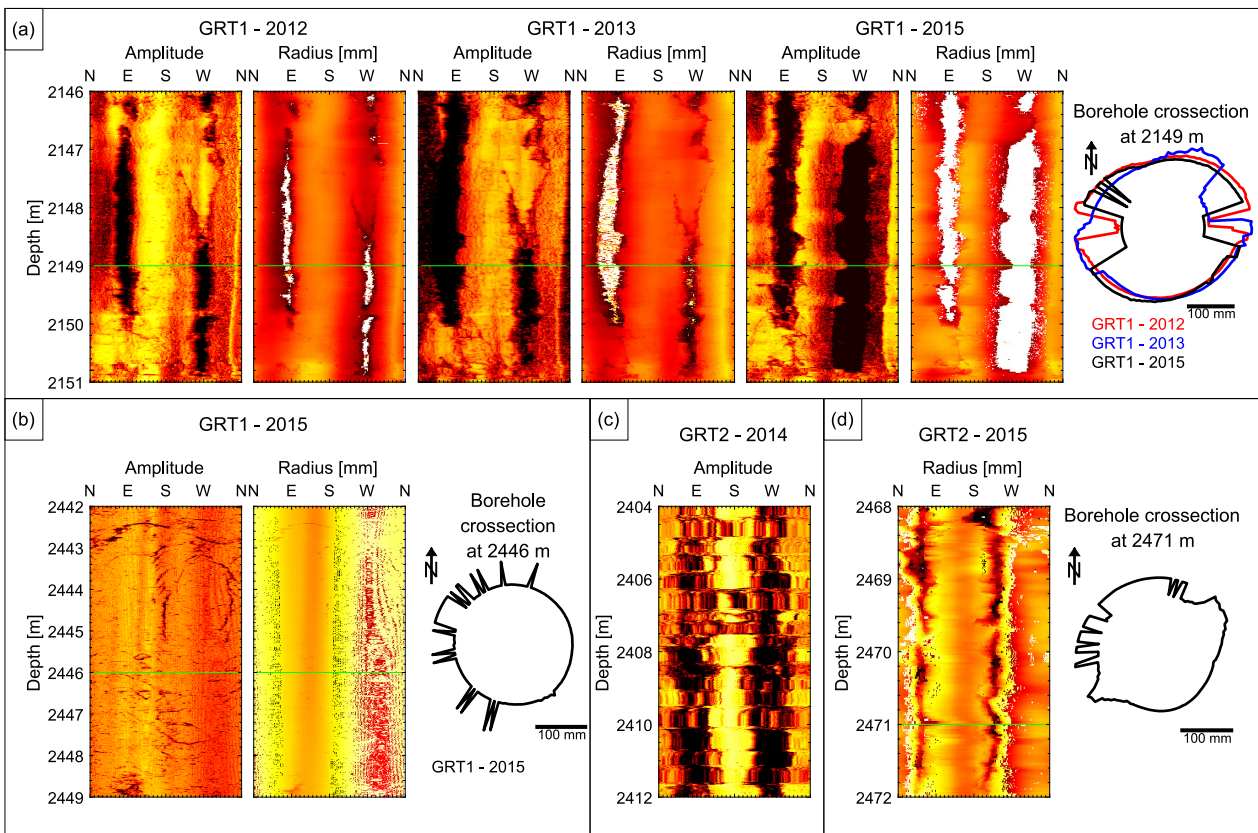




Figure 3: Example of image artefact observed on the GRT-1 and GRT-2 data set. a) Comparison of data from 2012, 2013 and 2015 collected in GRT-1 presenting a signal loss artefact in sandstones. b) Wood grain artefact visible on the 2015 GRT-1 image, both on the amplitude and radius image in granite. This leads to noisy borehole section. c) Stick-slip artefact present along the entire GRT-2-2014 image. d) Erroneous radius record observable on the GRT-2-2015 image in granite, possibly related to tool decentralization.

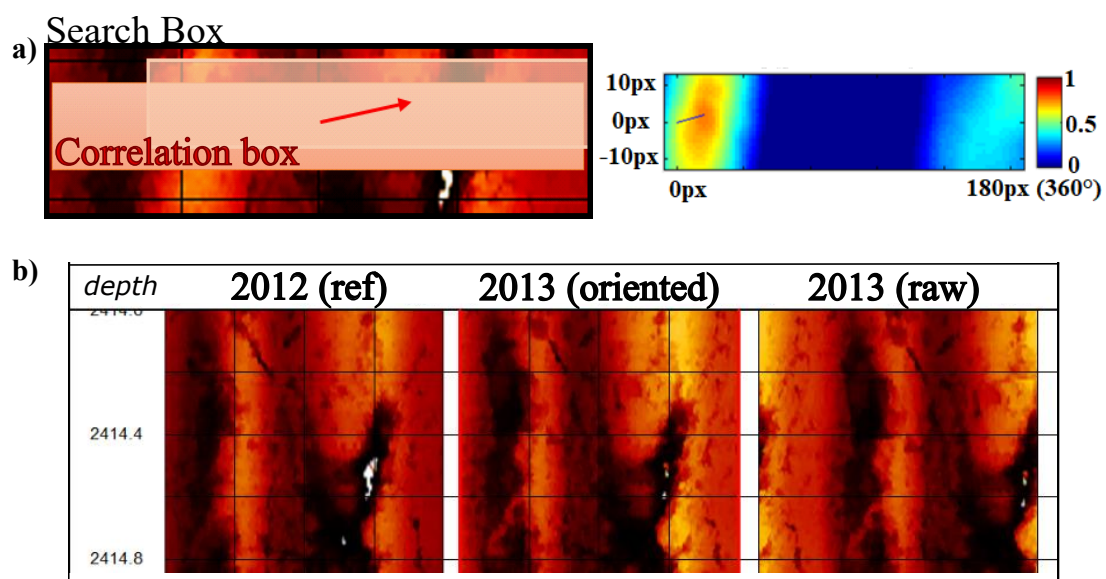




Figure 4: a) Sketch presenting the process used to orientate the images of GRT-1. A correlation box is defined in the double transit time image of reference (acquired in 2012) and is progressively shifted in the image to compare with (red windows) within the limits of the search box (black window). We compute the correlation between the correlation box in its initial position in the image of reference and the shifted correlation box in the image to compare with for each position (right insert). The displacement maximizing the correlation factor enables, at a given depth, to rotate and adapt the image of 2013 and 2015 according to the image of 2012. b) example of original and reoriented time transit images of 2013, at a depth of 2414m (TVD) in GRT-1.

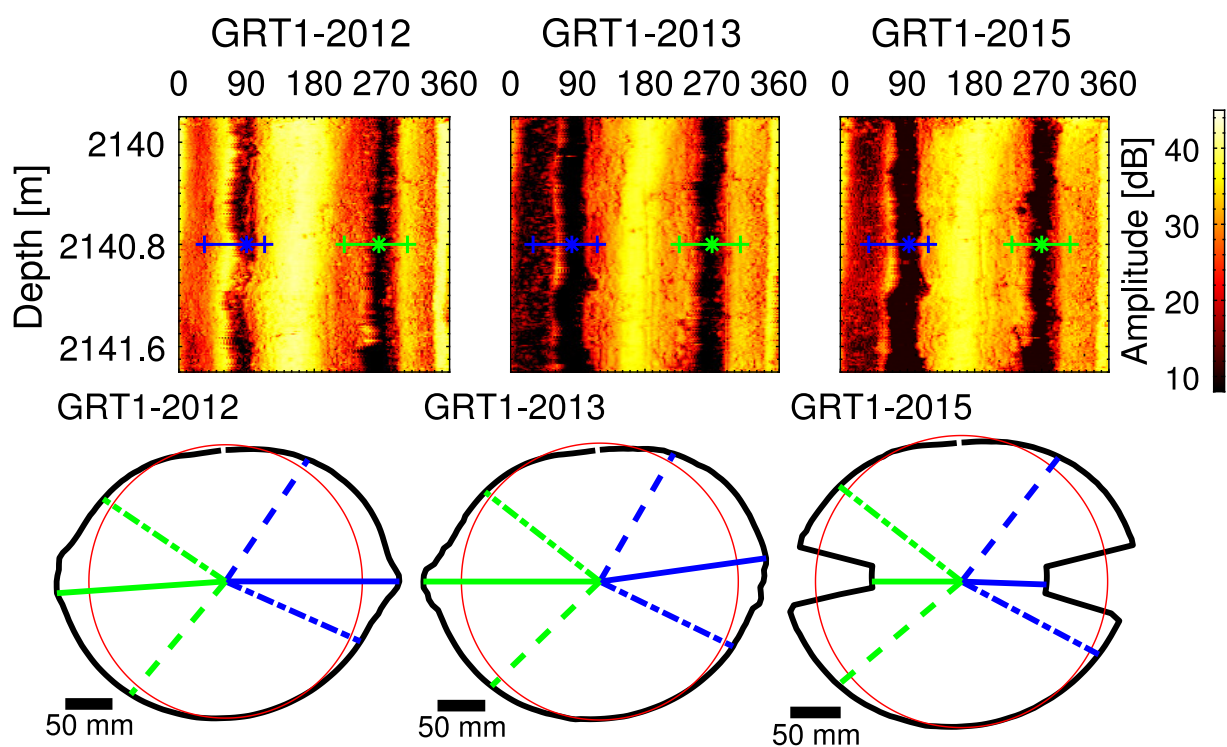




Figure 5: Example of breakout geometry determination in sandstones. Upper figures: amplitude images for GRT-1 at 2140.8 m for the logs from 2012, 2013 and 2015. Lower figures: wellbore section at 2140.8 m computed from the transit time images from the 2012, 2013 and 2015 logs respectively. The breakout extent is determined on the wellbore section. The blue and green dashed lines represent the extent of the breakout when the plain lines represent the azimuth of maximum radial extension of the breakout.

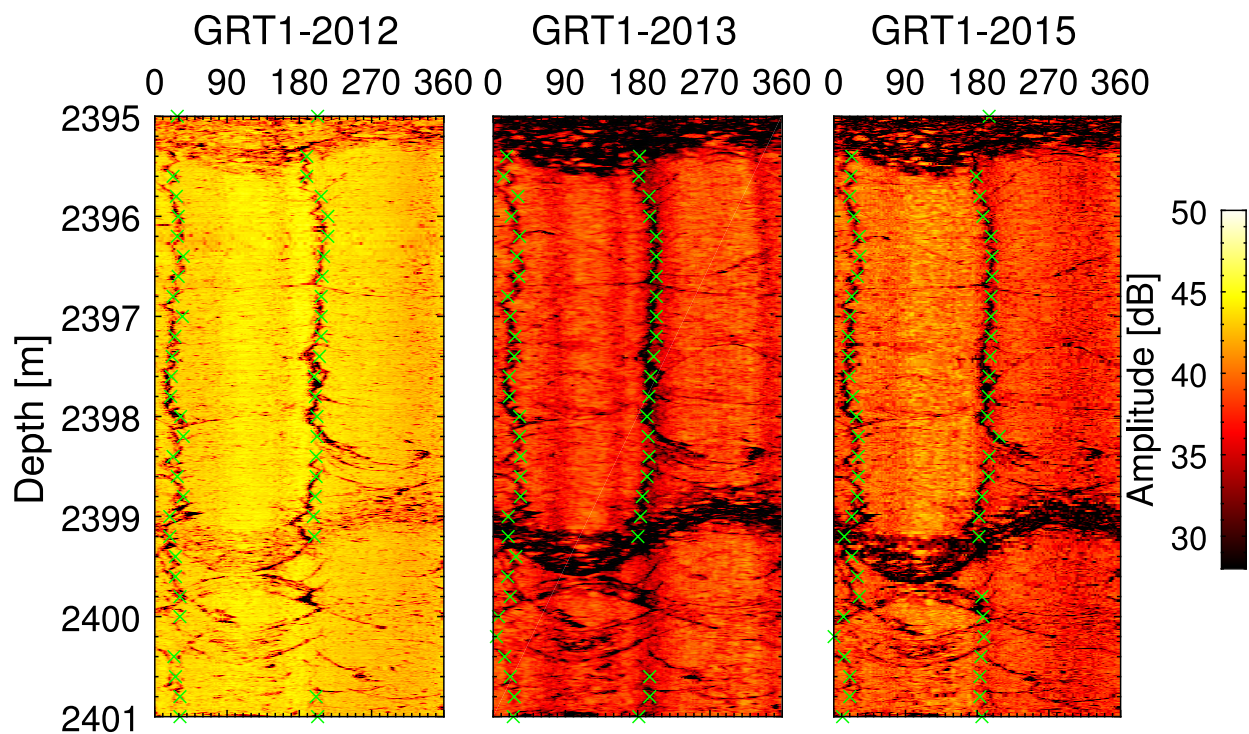




Figure 6: Examples of Drilling Induced Tension Fractures (DITFs), observed in the granitic section of GRT-1 in the amplitude images acquired in 2012, 2013 and 2015. The azimuth of the DITFs is measured every 20 cm (green crosses).

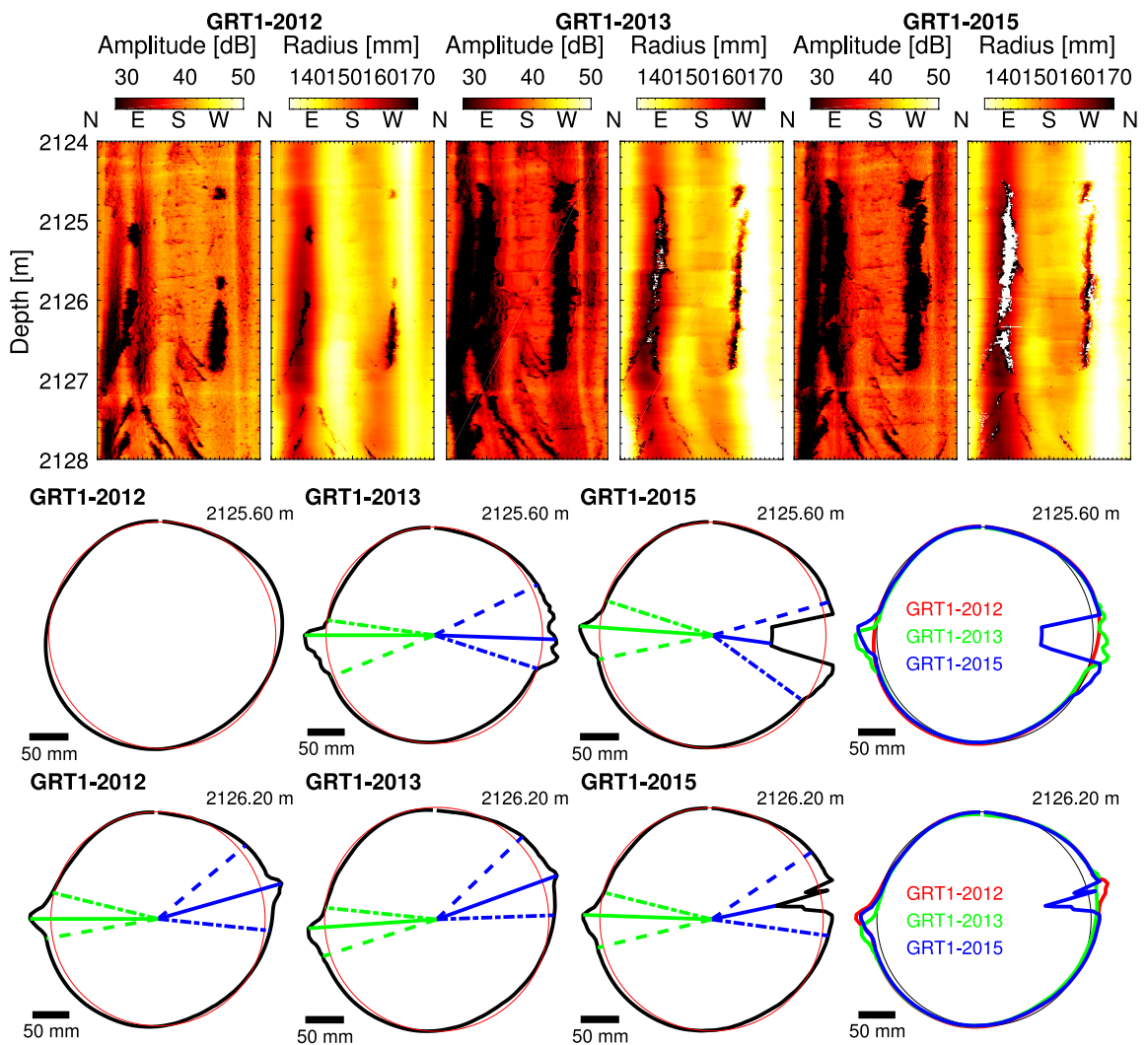




Figure 7: Examples of breakout shape evolution between the three successive images collected in GRT-1 in sandstones. Upper figures show the amplitude images and the radius computed from the time transit images for a section of GRT-1 from 2124 to 2128m (TVD) in 2012, 2013 and 2015. Lower figures show the mean section computed at 2125.6 and 2126.2m (TVD) from the time transit images averaged over 60cm intervals. The sections are represented along with an 8.5 inch radius circle representing the unaltered open hole section. The sections from the image of 2012, 2013 and 2015 are superposed in the right panel.

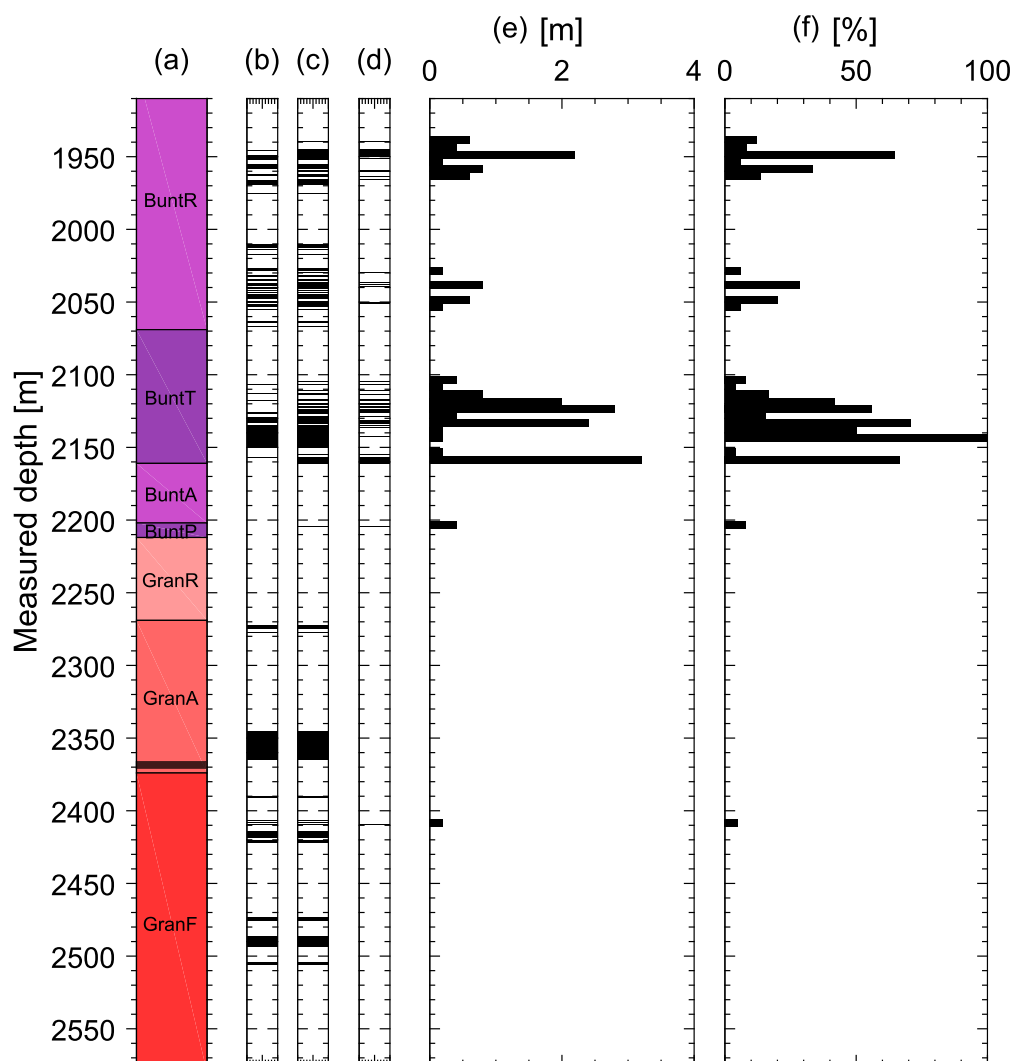




Figure 8: Development of breakouts along GRT-1 borehole between 2012 and 2013. a) Simplified lithologies along GRT-1 borehole with depth (MD): BuntR stands for “couches de Rehberg”, BuntT for “Couches de Trifels”, BuntA for Annweiler sandstone, BuntP for Permian layers older than Annweiler sandstone, GranR for rubefied granites, GranA for hydrothermally altered granite and GranF for low altered granite. The major fault zone crossing GRT-1 at 2368m is represented as a black band. b) Breakouts positions in GRT-1 in 2012. c) Breakouts positions in GRT-1 in 2013. d) Intervals where breakouts are present in 2013 but not in 2012. e) Breakout length increase in [m] along the borehole between 2012 and 2013 in 5 m bins. f) fraction in [%] of wellbore length that was free of breakout in 2012 that is presenting breakout on the 2013 image, computed in 5 m bins.

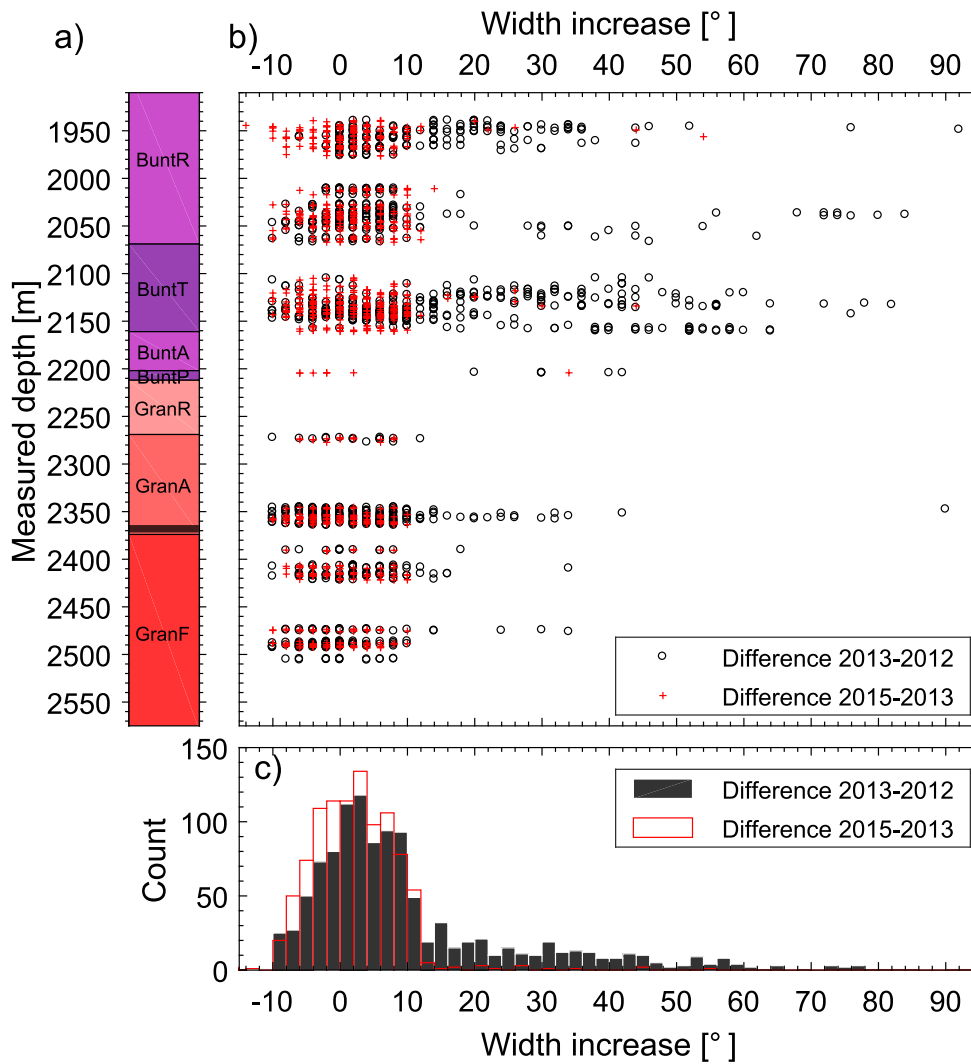




Figure 9: Evolution of breakout width in GRT-1 borehole with depth (MD). a) Simplified lithologies along GRT-1 borehole (see Fig. 8 for the legend). b) Width increase between the 2012-13 time interval (black circles) and the 2013-15 time interval (red crosses) presented as a function of the vertical depth. c) histograms in 2^5 classes of breakout width changes for the 2012-13 interval (black) and the 2013-15 interval (red).

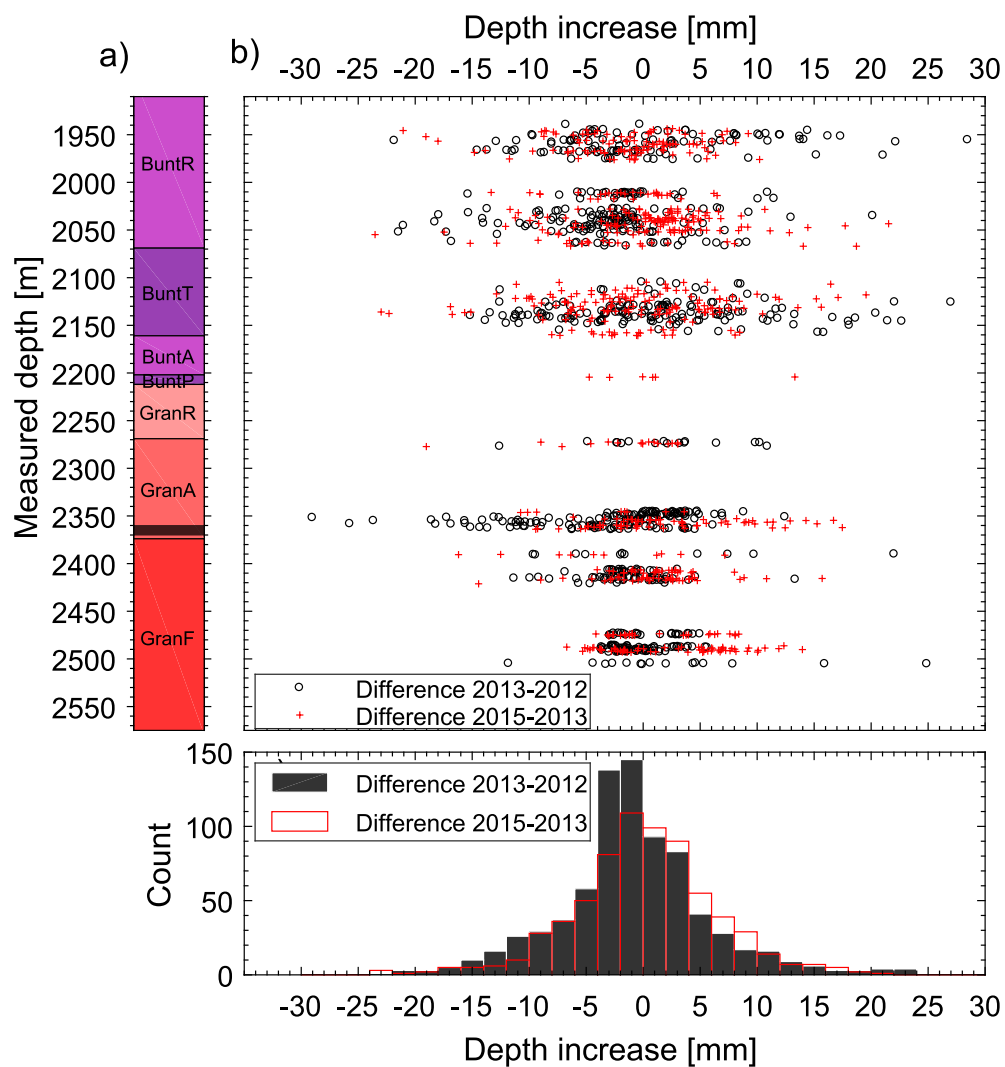




Figure 10: Evolution of the depth of the breakouts in the GRT-1 borehole with depth (MD). a) Simplified lithologies along GRT-1 borehole (see Fig. 8 for the legend). b) Increase of the maximum radial extension between the 2012-13 time interval (black circles) and 2013-15 time interval (red crosses) presented in function of depth. c) histograms in 2 mm classes of breakout with changes for the 2012-13 interval (black) and 2013-15 interval (red).

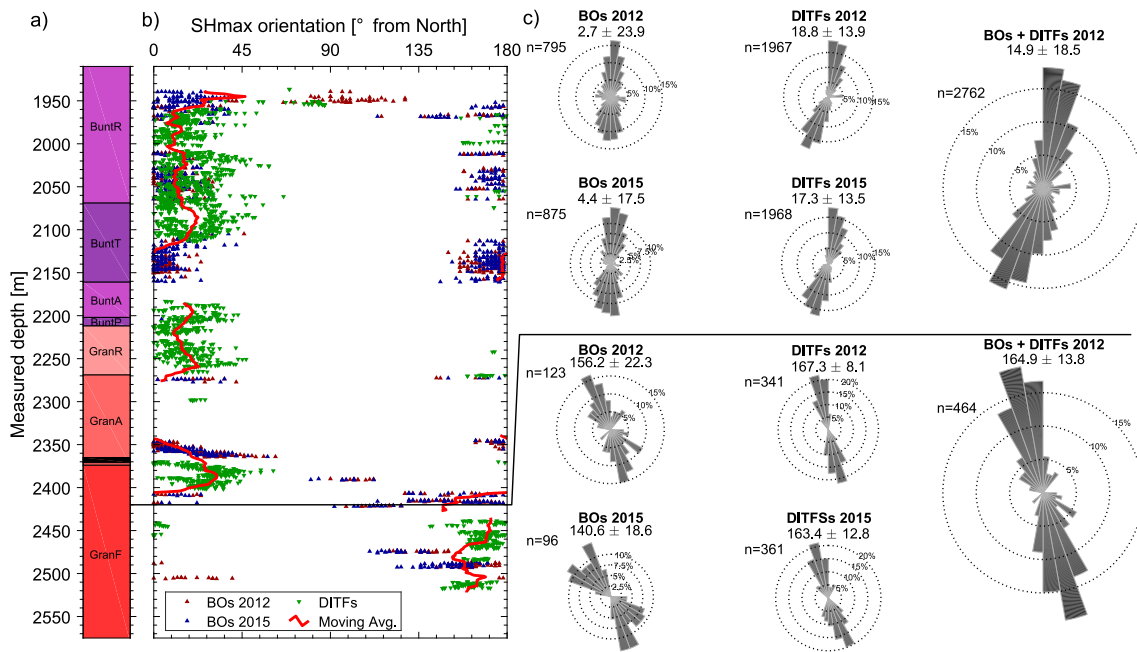




Figure 11: Evolution in orientation of the maximum principal stress with measured depth in GRT-1, in 2012 and 2015. a) Simplified lithologies along GRT-1 borehole (see Fig. 8 for the legend). b) Orientation of SH from the azimuth of maximum radial extension of the breakouts (BOs) from the dataset of 2012 (in blue) and of 2015 (in red) acquired in GRT-1. In green, orientation of SH from the azimuth of Drilling Induced Tensile Fractures (DITFs). The red line is a moving average of the orientation data. c) From the datasets displayed in panel b), orientation in rose diagrams.

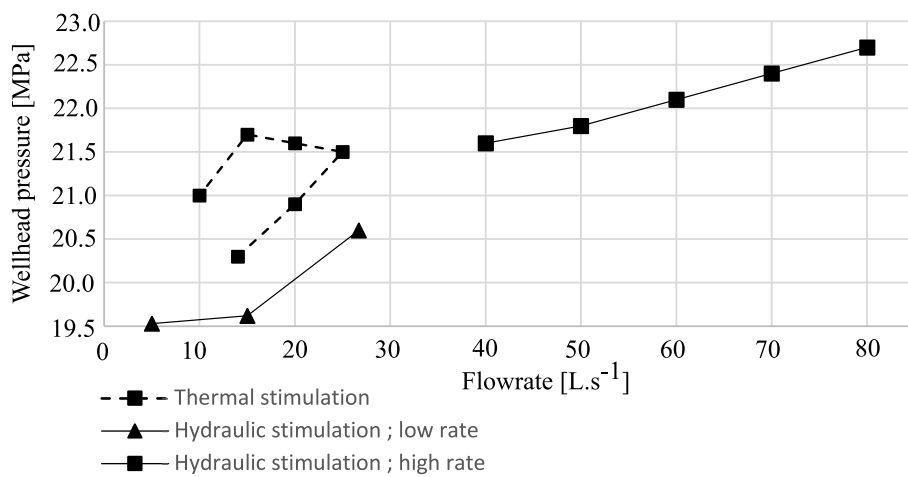




Figure 12: Minimal horizontal stress S_h [MPa] with depth at the Soultz-sous-Forêts site from three studies obtained from high-volume injections in GPK-1, GPK-2, GPK-3 and EPS-1 wells. The lower bound for the minimal horizontal stress S_h obtained from the analysis of the hydraulic stimulation of the well GRT-1 is represented for comparison (black circle).

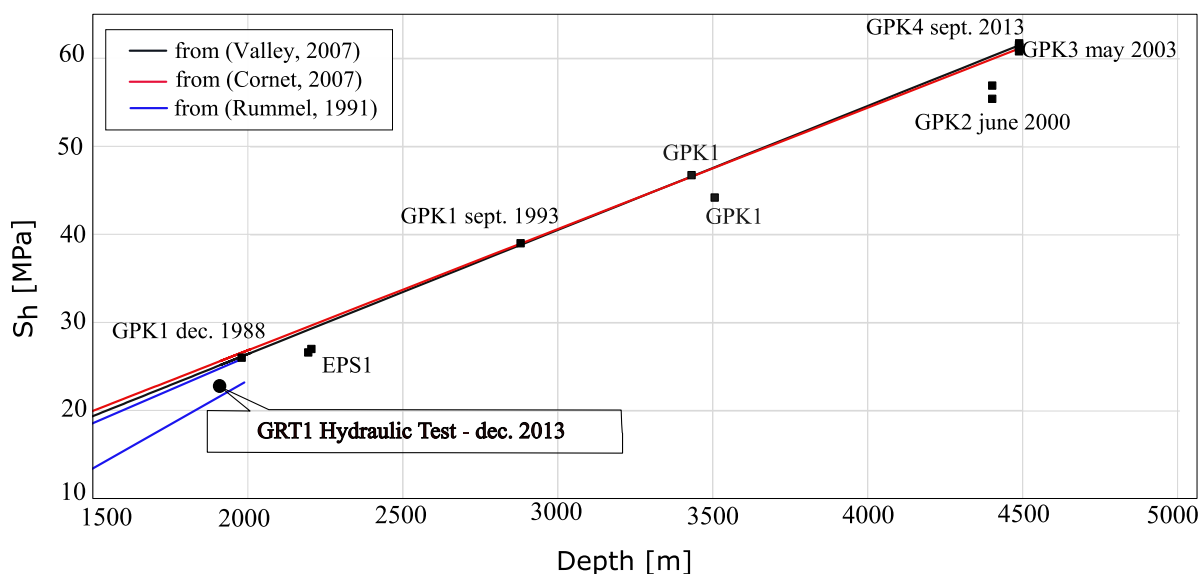




Figure 13: Stabilized wellhead pressure [MPa] for each flowrate step measured during the stimulation operations conducted in GRT-1 in 2013, targeting a depth of 1913 m (TVD), as a function of flow rate [$\text{L}\cdot\text{s}^{-1}$] (after Baujard et al., 2017).

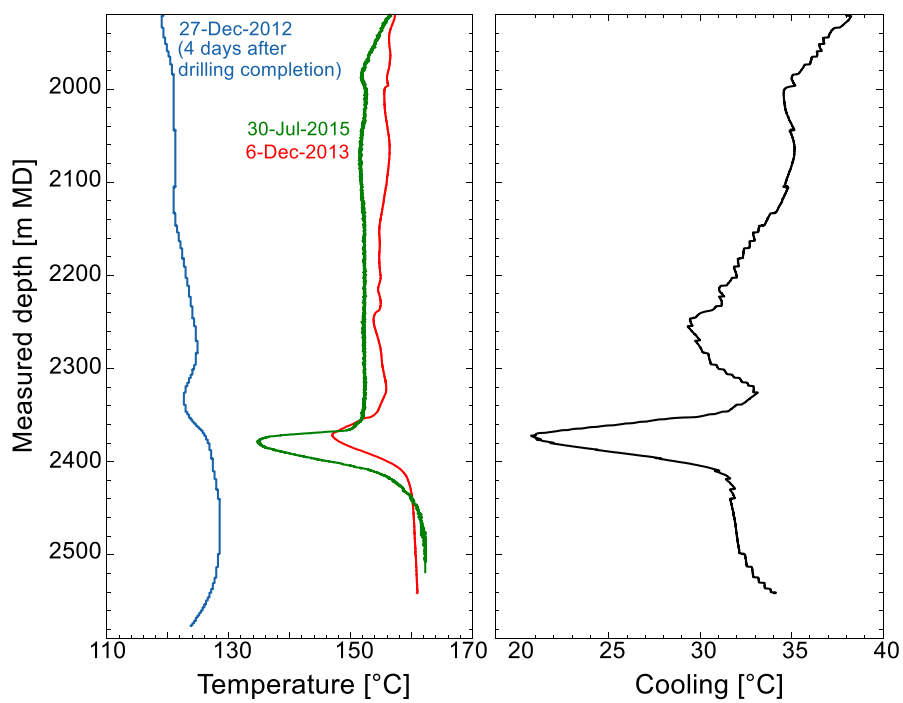




Figure 14: Left panel: variation of temperature [$^{\circ}\text{C}$] with depth (MD), estimated from the temperature log acquired in 2015 in GRT-1 (green curve), plotted along with the temperature log acquired in 2013 (red curve). The temperature log acquired four days after drilling completion (blue curve) enables to estimate the temperature at the borehole wall during drilling. Right panel: estimation of the difference in temperature between the wellbore temperature and the borehole wall temperature after completion Δt used in the evaluation of the thermal stress components.

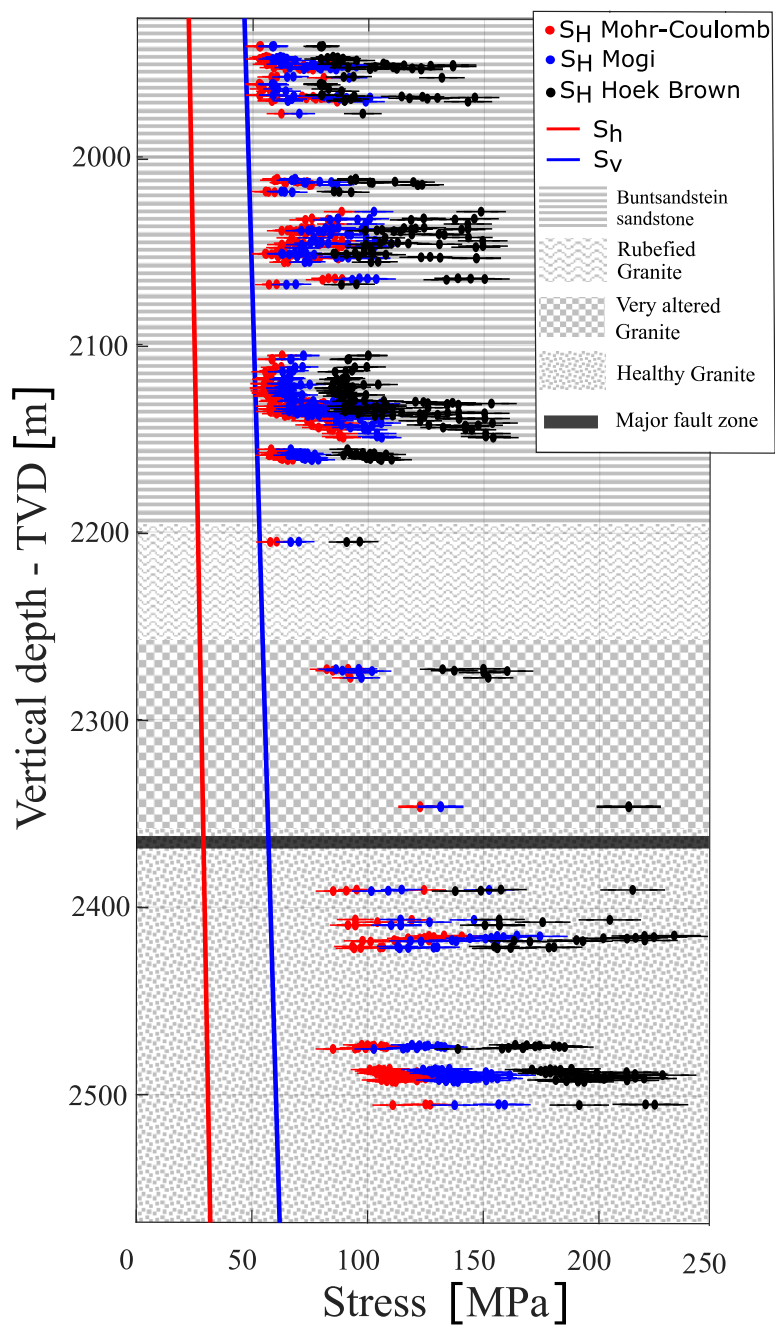




Figure 15: *in-situ* stress state components Sh , SV and SH [MPa]. Maximum horizontal stresses SH are inverted with three distinctive failure criteria for the images of 2013 of GRT-1 well. Error bars are calculated considering the error on the measurement of the breakout width, on the estimates of the elastic parameters and on the Sh and SV trends with depth. The background pattern represents the four major lithological units retained in the model and the major fault zone crossed by GRT-1.

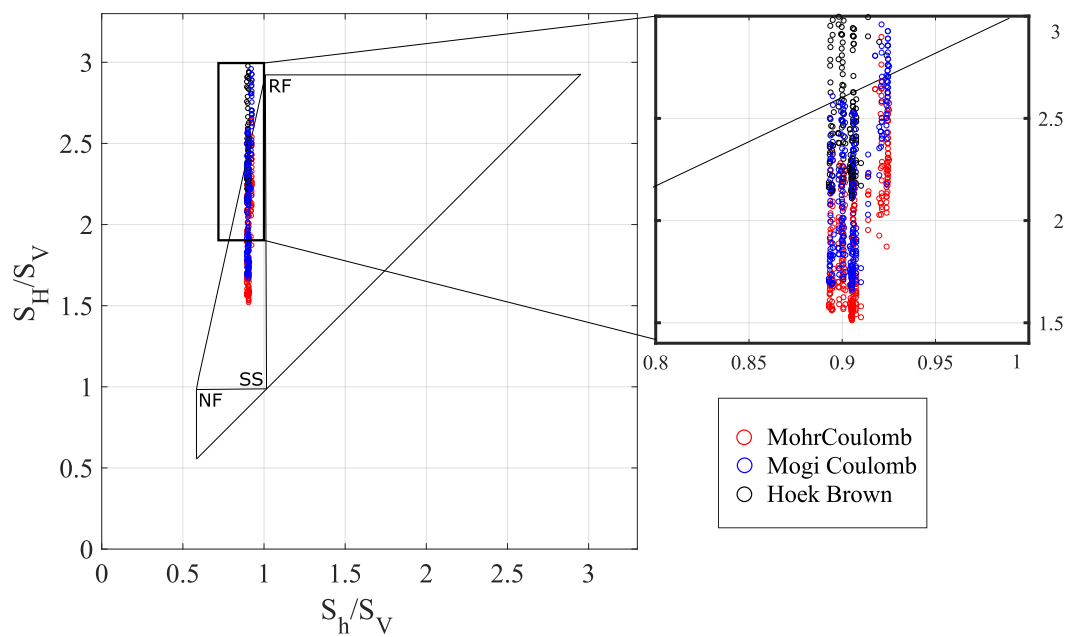




Figure 16: Normalized stress polygon defining stress states (SH/SV , Sh/SV) at a depth of 2500m in GRT-1, according to a Coulomb law with a coefficient of friction $\mu=1$. The borders of the polygon correspond to an active fault situation. According to Anderson's faulting theory, *RF* – reverse faulting – *SS* – strike slip regime – and *NF* – normal faulting – refer to the Anderson's faulting regimes. It is plotted along with the stresses (SH/SV – Sh/SV) calculated from the image of the GRT-1 of 2013, for three different failure criteria (circles in color).

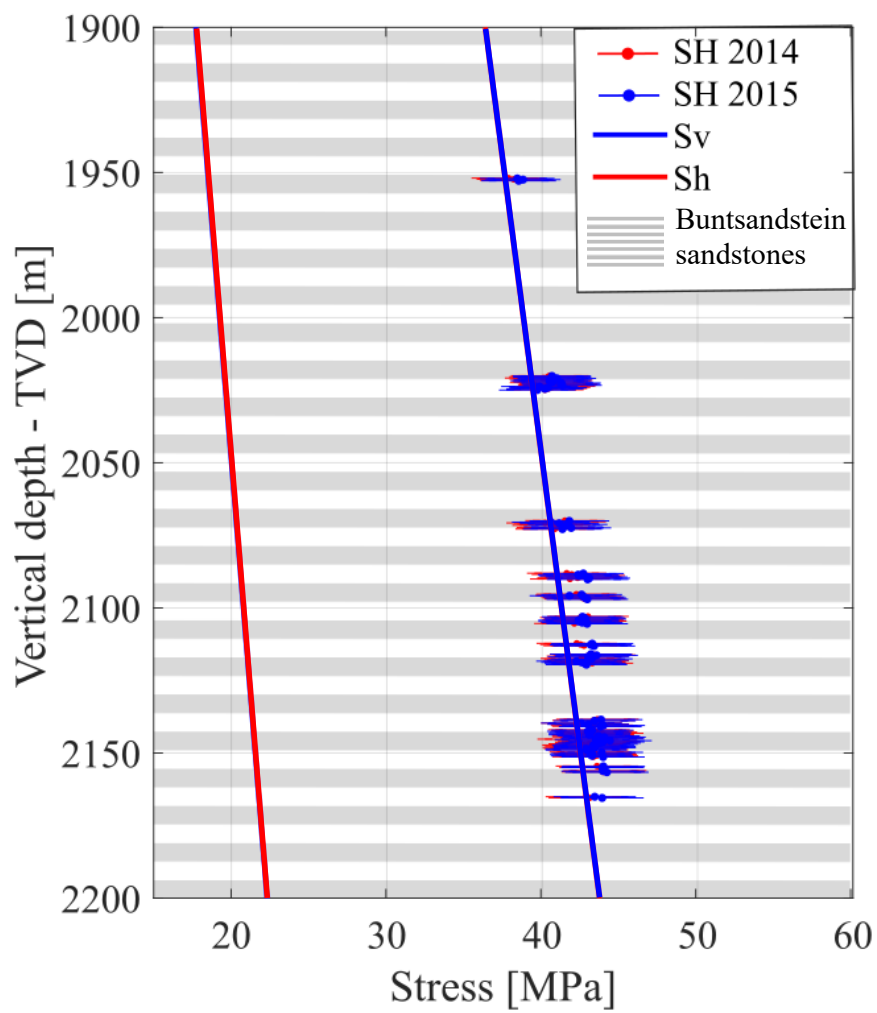




Figure 17: in-situ stress components S_h , S_v and S_H [MPa] in the deviated well GRT-2. S_H stresses are inverted using a Mohr Coulomb failure criterion and represented as a function of the vertical depth for the images acquired in 2014 and 2015. Error bars are calculated considering the errors on the measurements of the breakout widths, on the elastic parameters and on the S_h and S_v trends. The background pattern represents the major lithological unit crossed by the well.

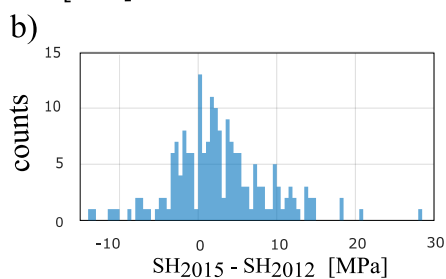
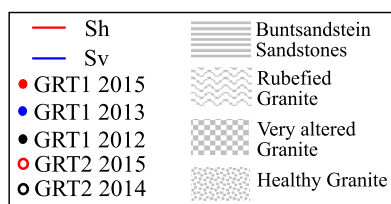
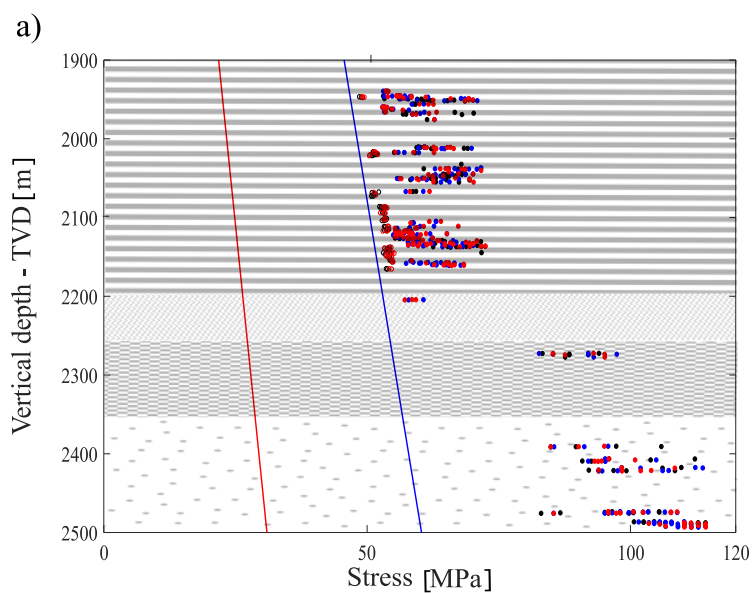




Figure 18: Panel a. shows the SH stresses [MPa] inverted with a Mohr-Coulomb criterion from the images acquired in 2012 – 2013 and 2015 (plain circles) in GRT-1 and in 2014 and 2015 (empty circles) in GRT-2, as a function of vertical depth. The background shows the lithological units retained in the model. Panel b. shows the difference in SH stresses between 2015 and 2012 in GRT-1 in a histogram with 1 MPa bins.

**Table 1: Data acquired in GRT-1 and GRT-2 and specificities of UBI acquisition programs.**

Well	Acquisition Date	Stimulation	Logging depth range [m; MD]	Transducer diameter [inch]
GRT1	30-Dec-2012	4 days after drilling completion	1913.00 - 2568.00	4.97
	9-Dec-2013	1 year after drilling completion 5 months after THC stimulation	1912.00 - 2531.16	2.92
	30-Jul-2015	2.5 years after drilling completion 2 years after THC stimulation.	1910.96 - 2499.9	4.97
GRT2	23-Jul-2014	Four days after drilling completion	2118.00 - 2531.22	4.97
	29-Jul-2015	1 year after drilling completion	2111.00 - 2869.23	4.97

Table 2: Elastic (Poisson ratio) and strength parameters (used in the Mohr-Coulomb, Mogi-Coulomb and Hoek Brown failure criteria) for the four geological units retained in the model, for both GRT-1 and GRT-2 wells, as a function of measured depth (MD). Elastic and strength parameters for granites are based on a data compilation of tests conducted on samples from Soultz-sous-Forêts. For the Buntsandstein sandstones, we use usual strength parameters based on Hoek & Brown (1997).

Depth (MD) [m] GRT1	Depth (MD) [m] GRT2	Geology		Elastic and strength Parameters					
		Stratigraphy	Lithology	ν	Cohesion C [MPa]	Internal Friction θ	UCS [MPa]	(a, b) Mogi Coulomb	Hoek Brown m_i
1799-2212	2022-2479	Bunt-sandstein	Sandstones (argilic)	0.22	24 ±5	35°	92±14	(18 ±3, 0.54)	19
2212-2269	2479-2629	Granitic Basement	Ruberfied Granite	0.26	23 ±5	40°	100 ±15	(13 ±3, 0.68)	20
2269-2374	2629-2881		Hydrothermally altered Granite	0.26	29 ±5	40°	125 ±17	(17 ±3.5, 0.68)	23
2374-2580	2881-3196		Low altered Granite	0.26	32 ±5	45°	155 ±20	(21 ±3.5, 0.68)	27



Table 3: Mean density retained for each lithological layer and vertical depth (TVD) in each well.

Description	Depth in GRT1 [m]	Depth in GRT2 [m]	Volumetric mass [kg.m ⁻³]
Tertiary	0	0	2350
	1172	1166.5	
Jurassic	1172	1166.5	2440
	1447	1431.5	
Keuper	1447	1431.5	2700
	1653	1637	
Muschelkalk	1653	1637	2750
	1798	1793.5	
Top Buntsandstein	1798	1793.5	2610
	1855	1850	
Mean Buntsandstein	1855	1850	2520
	2147	2109	
Bottom Buntsandstein	2147	2109	2540
	2198	2167	
Granitic basement	2198	2167	2570
	2568	2707.5	